Manuscript draft submitted to Climate Dynamics, 30 september 2005

Description and validation of the CNRM-CM3 global coupled model

D. Salas-Mélia, F. Chauvin, M. Déqué, H. Douville, J.F. Guérémy, P. Marquet, S. Planton, J.F. Royer and S. Tyteca

Centre National de Recherches Météorologiques, Météo-France,
42 avenue G. Coriolis, 31057 Toulouse, France

Abstract

The Centre National de Recherches Météorologiques Coupled global climate Model, version 3 (CNRM-CM3) is described. It is based on the coupling of ARPEGE-Climat version 3 AGCM, OPA8.1 ocean model, GELATO2 sea ice model and TRIP river routing scheme. CNRM-CM3 was applied to carry out several climate simulations in the framework of the IPCC fourth assessment report, all of them without flux correction. Among these experiments, the 500-yr preindustrial control and a historical simulation of the 1860-2000 period are analysed in this study, in terms of mean climate, drift and variability. Compared to the model's previous version (CNRM-CM2), the simulated ocean circulation is improved, which is due to a better modelling of deep convection, particularly in the North Atlantic, and sea ice is realistic in both hemispheres. However, the ocean surface is generally too cold in both simulations compared to available observations, especially in the tropics, and the simulated global climate is colder and wetter than observed, even if biases are smaller by the end of the 20th century. Reasons for these aspects of the simulations were investigated and an outline of further needed model developments is given.

1. Introduction

The first coupled model including ARPEGE-Climat was developed by CERFACS (Terray *et al.*, 1995; Barthelet *et al.*, 1998; Guilyardi *et al.*, 2001), as its second version was coupled with OPA7 OGCM by means of the OASIS software. It has been used for the CMIP project (Meehl *et al.*, 2000; Covey *et al.*, 2000; Lambert and Boer, 2001; Jia, 2003) and in other intercomparisons of coupled models (Pontaud *et al.*, 2000; Davey *et al.*, 2002; Frankignoul *et al.*, 2004). Merging this initial model with the development of a coupled ocean-sea ice model (OPA8.0-GELATO2, Salas-Mélia, 2002) led to CNRM-CM2 numerical coupled climate system. CNRM-CM2 has been used to perform climate change scenarios (Royer *et al.*, 2002) that have been analysed in several recent publications (Douville *et al.*, 2002; Maynard *et al.*, 2002; Ashrit *et al.*, 2003; Camberlin *et al.*, 2004; Douville, 2005). This coupled version has also been applied for studies of tropical deforestation (Voldoire and Royer, 2005). Another coupled version similar to CNRM-CM2, but with a climatological sea ice formulation instead GELATO2, has also been used for seasonal forecasting experiments in the DEMETER project (Palmer *et al.*, 2004; Guérémy *et al.*, 2005).

CNRM-CM3 coupled general circulation model is the sum of the updated version of the different model components already present in CNRM-CM2. In particular, a more

adequate turbulence scheme was applied in ARPEGE-Climat in very stable cases. The new aerosol and greenhouse forcings used as input data are described in sections 3.1 and 3.2. The new system includes ARPEGE-Climat 3, which is the atmospheric part of the system (developed at CNRM), OPA8.1 ocean model (IPSL/LOCEAN, Paris, France), GELATO2 dynamic and thermodynamic sea ice model (CNRM) and TRIP river routing scheme (University of Tokyo, Japan). These models are coupled together with OASIS2.2 (CERFACS). This software ensures that space interpolations between the different model grids and time synchronisation of the models are correct. More details are given about every component of CNRM-CM3 in the following sections.

2. Model description

2.1. The Atmospheric General Circulation Model: ARPEGE-Climat 3

Since its first version described by Déqué *et al.* (1994), the ARPEGE-Climat atmospheric GCM has been used in various climate sensitivity experiments (Douville, 2002 ; Douville, 2003; Masson *et al.*, 2003 ; Douville, 2004 ; Maynard and Royer, 2004b ; Voldoire and Royer, 2004 ; Chauvin *et al.*, 2005). The ARPEGE-Climat model has also participated to intercomparison projects such as AMIP (Gates *et al.*, 1999) and PMIP for paleoclimatic simulations at 6000 BP (Joussaume *et al.*, 1999). A variable resolution version of ARPEGE-Climat using a stretched grid for increasing the resolution over a region of interest has been developed (Déqué and Piedelievre, 1995) and applied to climate simulations over Europe (Déqué *et al.*, 1998; Gibelin and Déqué, 2003; Hagemann *et al.*, 2004; Terray *et al.*, 2004), or over tropical regions (Lorant and Royer, 2001; Moustaoui *et al.*, 2002; Maynard and Royer, 2004a).

ARPEGE-Climat version 3 is fully described in Déqué *et al.* (1999) and Gibelin and Déqué (2003), however its major features are briefly summarized here. In ARPEGE-Climat, the representation of most model variables is spectral (i.e. scalar fields are decomposed on a truncated basis of spherical harmonic functions). In the framework of this study, it was used on a horizontal grid corresponding to a T63 triangular truncation. All the physics and the treatment of model nonlinear terms require spectral transforms to a Gaussian grid. This 128x64 grid (about 2.8° resolution in longitude and latitude) is reduced near the poles, in order to obtain more grid-point isotropy than with a classical regular longitude-latitude grid and save computational time. The vertical levels are defined with a progressive hybrid sigma-pressure vertical coordinate including 45 layers, in order to correctly represent the atmospheric circulation in the stratosphere, where the maximum of ozone concentration is found (23 pressure levels lie above 200hPa and the topmost layer is located at 0.05hPa). There are 7 layers below 850hPa, except in regions of high orography. The time integration is semi-implicit, with a time-step Δt_a of 30mn, except for the radiative transfer (3h time-step). The use a two time level semi-lagrangian advection scheme in ARPEGE-Climat reduces computational costs and makes filtering of $2\,\Delta t_a$ numerical waves unnecessary. The model includes six prognostic variables: temperature, specific humidity, ozone concentration, surface pressure, vorticity and divergence (northward and eastward wind components would raise a definition problem at the poles). The role of sea salt, desert dust, black carbon and sulfate aerosols on

solar/longwave radiation is taken into account by specifying concentrations for these different species. However, their indirect effects are not considered in this version of the model. More details about the aerosol data used are given in section 3.2.

The main parameterizations used by ARPEGE-Climat are summarized in table 1. Note the soil and vegetation surface scheme ISBA is included in ARPEGE-Climat (described specifically in section 2.4.)

Parameterization	Reference
SW and LW radiation schemes : Foucart and Morcrette parameterizations	Morcrette (1990); Morcrette (1991)
Clouds, large-scale precipitation and vertical diffusion: statistical diagnostic scheme.	Ricard and Royer (1993) ; Mascart *et al.* (1995)
Convection : mass-flux convective scheme with Kuo-type closure	Bougeault (1985)
Ozone	Cariolle and Déqué (1986) ; Cariolle *et al.* (1990).
Surface scheme (ISBA)	Described in section 2.4

Table 1: The main parameterizations in ARPEGE-Climat version 3.

2.2. The Oceanic General Circulation Model: OPA8.1

OPA 8.1 ocean model was developed by IPSL/LOCEAN (Paris, France) and is described in detail by Madec *et al.* (1998). In the framework of CNRM-CM3 it is used in its global configuration (182x152 points on the horizontal, without any North Pole singularity), i.e. about 2° resolution in longitude, while in latitude, its resolution varies from 0.5° at the equator to roughly 2° in polar regions (see Madec and Imbard, 1996 for a geometrical definition). On the vertical, a z-coordinate (31 vertical levels with 10 levels in the upper 100 m) is used. The mesh is an Arakawa-C grid. The chosen time step was 5760s (15 time-steps per day). This is the maximum time-step both ensuring numerical stability and permitting an integer number of time steps per day. OPA8.1 is a rigid lid model using a virtual freshwater flux as an input for the vertical salt diffusion scheme. Near the coast, this freshwater flux includes river discharge computed by TRIP river routing scheme (see section 2.4).

To account for the contribution of icebergs to the water cycle, a climatological, constant water flux is introduced south of 60°N during the calving season (October through April), as well as a constant heat flux corresponding to the energy necessary to melt the equivalent volume of ice. More details about this simple method are given in section 2.4 about surface schemes. The vertical diffusion of temperature uses the atmospheric non-solar heat flux at the ocean surface as a boundary condition. These diffusion schemes are implicit, while the non-diffusive part of the physics is treated in leapfrog. In this version, the advection is upstream.

The prognostic variables are the horizontal velocity field and thermohaline variables. The vertical component of ocean velocity is diagnosed from the horizontal components by using the continuity equation. Vertical eddy diffusivity and viscosity

are computed from a 1.5 TKE turbulent closure scheme (Blanke and Delecluse, 1993), while on the horizontal an isopycnal diffusion scheme is applied, with an eddy viscosity of 40000 m2/s for momentum and an eddy diffusivity equal to 2000 m2/s for tracers. The penetration of sunlight is formulated by means of two extinction coefficients (Paulson and Simpson, 1977), with values corresponding to a type I water in Jerlov's classification. At the bottom of the ocean, the fluxes of heat and salt are set to zero as boundary conditions, and a linear friction for momentum is hypothesized.

2.3. The sea ice model: GELATO 2

GELATO model was developed at CNRM and its second version is described in detail by Salas-Mélia (2002). It can be used on any generalized orthogonal curvilinear grid, but here it was run on the same horizontal grid as OPA's, in order to avoid unnecessary interpolations and singularities at the North Pole. The time step is 24h. GELATO 2 is a multi-category ice model (thickness dependant), allowing a more precise treatment of thermodynamics, since the growth rates of ice slabs of different thicknesses, subjected to the same oceanic and atmospheric forcings can vary considerably from one category to another. In other words, within a grid cell, sea ice is described as a collection of ice slabs, and each slab is described by its thickness, the fraction of the grid cell it occupies, its enthalpy, and the amount of snow covering it (sea ice salinity is constant at 6 psu). In order to model vertical heat diffusion in an ice-snow slab, a vertical discretization is defined, considering four layers in the ice part of the slab and one level in snow. Solving of this diffusion scheme is implicit in time. The rest of the thermodynamics, including a snow aging scheme (described in Salas-Mélia, 2002) is treated explicitly.

In CNRM-CM3, four categories were considered, as sensitivity experiments carried out with GELATO with more categories did not turn out to produce significantly different results, in agreement with Bitz *et al.* (2001). The different sea-ice categories are: 0-0.3m, 0.3-0.8m, 0.8-3m, and 3m or more. Transitions between these categories may occur as ice slabs melt or increase in thickness. If two or more slabs happen to fall into the same thickness category, they are merged together, conserving snow and ice mass as well as enthalpy.

For sea ice dynamics, the elastic-viscous-plastic rheology (Hunke and Dukowicz, 1997) is used. Advection of sea ice is semi-lagrangian, as described in Hunke *et al.* (2002). A redistribution scheme, based on Thorndike *et al.* (1975) and including the rafting and ridging of sea ice is coupled to the dynamics, as described by Salas-Mélia (2002). Note that transitions between sea ice categories may also occur as slabs are deformed due to redistribution processes.

Consistently with the rigid lid assumption made in the ocean component of CNRM-CM3, the salinity concentration effect concerning surface ocean water due to the freezing of sea ice is taken into account by computing a virtual freshwater flux.

2.4. Land surface processes in CNRM-CM3: ISBA and TRIP

The land surface scheme ISBA (Interactions Soil Biosphere Atmosphere) was initially developed by Noilhan and Planton (1989) and was first introduced in the CNRM climate model by Mahfouf *et al.* (1995). It is a relatively simple scheme that contains the basic physics of the land surface processes, but needs only a minimum of parameters. Soil and vegetation properties are derived from the global high-resolution ECOCLIMAP dataset (Masson *et al.* 2003) after aggregation onto the ARPEGE horizontal grid. Both the distribution and phenology of the vegetation cover are prescribed and do not interact with climate variability. A snow scheme, described in Douville *et al.* (1995a and 1995b), is used to compute the evolution of snow mass, snow albedo and snow density in each grid cell. In the presence of snow, the ECOCLIMAP snow-free albedo is modified according to a diagnostic snow fraction depending on snow mass, vegetation roughness length and subgrid orography. In the present study, the minimum and maximum snow albedo have been slightly decreased (0.45 and 0.80 respectively) compared to Douville *et al.* (1995b).

ISBA computes a single surface energy budget using a composite surface temperature. Four layers are used to describe the vertical profile of soil temperature. The soil hydrology is based on the force-restore approach, with a prognostic surface reservoir included in the total reservoir (Noilhan and Planton 1989). Compared to the original version of ISBA, CNRM-CM3 includes a deep drainage (Mahfouf and Noilhan, 1996) that has been here slightly modified to account for a residual drainage below the field capacity. Moreover, a sub-grid runoff has also been introduced based on the Variable Infiltration Capacity approach (Chapelon *et al.* 2000). Total runoff is interpolated on a 1° by 1° horizontal grid by means of the OASIS coupler (see section 2.5 for further details about coupling methods) to be converted into river discharge and transported to the ocean using the TRIP (Total Runoff Integrated Patways) river routing scheme developed by T. Oki (Oki and Sud, 1998; Chapelon *et al.* 2002). The water outflow produced at any river mouth is delivered at the nearmost ocean grid cell. As this amount of water can be huge for the biggest rivers, it is shared between several grid cells (up to 10 for the Amazone) to avoid unphysical ocean surface salinities. The timestep used in TRIP in the framework of CNRM-CM3 is 3h.

Ice sheets over Greenland and Antarctic are represented by initially prescribing a huge amount of snow and applying ISBA's standard snow parameterization. No ice dynamics is included in this ice sheets scheme. However, in order to close the water cycle, a climatological calving of icebergs was taken into account around the Antarctic (not Greenland). During the summer season (October to March), a constant flux of ice (0.14 Sv, i.e. 0.07 Sv annually) is calved at the coast. This climatological value was estimated from a preliminary coupled control run in which the climatological quantity of snow accumulating over the Antarctic in one year was diagnosed, which is equivalent to neglecting the interannual variability and trend of snow accumulation on ice caps. The corresponding mass of snow was found to be in the range of current estimates of the total mass of ice calved in the Antarctic seas per year. This approximation is valid as long as ice sheets are in steady state, i.e. if they do not significantly shrink or spread, which should be the case in the framework of preindustrial, historical (1860-2000) or 21st century climate simulations.

2.5. The coupling

Three different meshes are used within CNRM-CM3: a linear T63 grid, an irregular grid of about 2°x1° resolution, and a regular 1°x1° grid for respectively ARPEGE-Climat/ISBA, OPA-Gelato and TRIP. This means interpolations are needed so that the different models could exchange data. These field transformations are managed by OASIS coupler version 2.2, which also allows the three corresponding programs to run in a synchronous way. This software was developed at CERFACS (Toulouse, France) and is described by Terray *et al.* (1998). Table 2 lists the fields exchanged between the different models and, if OASIS is used, the kind of interpolation that is applied.

It should be noted that the remapping scheme used ensures water and heat conservation between source and target grids. Some subgrid variability is introduced after interpolation of fluxes from the atmospheric grid to the higher resolution ocean grid. The reason for this is that through remapping several contiguous ocean grid cells with different sea surface temperatures (SST) can get the same flux data from a common atmospheric grid cell, which is not physically consistent. Let T_0 be the spatially averaged SST of all oceanic grid cells lying under this particular atmospheric grid cell, ϕ_0^{ns} the atmospheric flux computed by ARPEGE-Climat in this area, and $\partial\phi^{ns}/\partial T$ the derivative of this flux by SST. For any concerned grid cell of SST T, the input surface heat flux can be defined as:

$$\phi^{ns} = \phi_0^{ns} + \partial\phi^{ns}/\partial T(T - T_0), \quad (1)$$

conserving the total flux while adding flux spatial variability. Where there is sea ice, GELATO sea ice model generally considers the surface is composed of four ice categories and open water, each of them having its own surface temperature and albedo. So in this case a similar linear repartition of the total non-solar heat flux is applied. This approximation may seem to be arguable as the temperature difference between ice covered areas and open water parcels within the same grid cell is sometimes as large as 40°C. However, it was checked that even in this case, the difference between an exact calculation over each grid cell and the result of repartition is reasonable. A linear repartition of the net short wave flux was also applied. For a given grid cell, if α_0 and ϕ_0^s are respectively the averaged surface albedo of the cell, and the average net shortwave flux provided by ARPEGE-Climat as an input to the ocean-sea ice model, the shortwave flux absorbed by a surface type of albedo α will be:

$$\phi^s = \frac{(1-\alpha)}{(1-\alpha_0)}\phi_0^s. \quad (2)$$

As the timestep for coupling is 24h, each quantity to be exchanged is first averaged on a daily basis in every source model before it is sent to the corresponding target model.

Source/Target model	Quantities exchanged	Interpolation type
Atmosphere-Ocean	Non-solar and solar heat fluxes, net water flux, wind stress components, non-solar heat flux derivative by temperature	Conservative remapping + subgrid variability, except for vectors (bicubic)
Atmosphere-Sea Ice	Non-solar and solar heat fluxes, evaporation, liquid and solid precipitations, wind stress components, non-solar heat flux	Conservative remapping + subgrid variability, except for vectors (bicubic)

	derivative by temperature	
Atmosphere-Land Surface	Radiative and turbulent fluxes	-
Land Surface-Atmosphere	Surface albedo, roughness, temperature, soil moisture	-
Land Surface-River Routing	Runoff	Conservative remapping
Ocean-Atmosphere	Temperature	Conservative remapping
Ocean-Sea Ice	Ocean heat flux, ocean surface current horizontal components, ocean surface temperature and salinity	-
Sea Ice-Atmosphere	Sea ice surface temperature, albedo and concentration	Conservative remapping
Sea Ice-Ocean	Non-solar and solar heat fluxes, net water flux, momentum	-
River Routing-Ocean	Water input at river mouths	Nearest neighbour with water conservation

Table 2: The main parameterizations in ARPEGE-Climat version 3.

3. The experiments

The experiments presented in this study are part of the simulations included in the IPCC database, in preparation of the IPCC's fourth assessment report. Since the scope of this paper is a presentation of CNRM-CM3, rather than a complete description of large number of climate simulations, we make the choice to focus mainly on the simulation of the 20th century (20C3M) and the control experiment, even if more experiments were carried out: IPCC-SRES B1, A1B, A2 simulations of the 21st century, stabilizations of A1B and B1 scenarios over the 22nd and 23rd centuries, 1% increase to doubled and quadrupled equivalent atmospheric CO_2 concentration experiments, and 150 year stabilizations at 2xCO_2 and 4 xCO_2 levels. The data is available after registration on http://www.cnrm.meteo.fr/dods/.
The experiments were all run with exactly the same version of CNRM-CM3 and with the same solar constant of 1370W.m^{-2}. Only the concentrations of greenhouse gases, sulfate and black carbon vary as a function of time. No surface flux adjustment was applied in the coupled model.

3.1. The concentration of greenhouse gases

The concentration of greenhouse gases is specified as annual mean values derived from observations for the period 1860-2000 and from IPCC SRES scenarios for the period 2000-2100. The main greenhouse gases explicitly taken into account in the radiative model are carbon dioxide (CO2), methane (CH4), nitrous oxide (N2O), and chlorofluorocarbons CFC-11 and CFC-12. The concentration of CFC-11 has been increased so as to include the equivalent radiative forcing due to the combination of the other minor species of CFCs, perfluorocarbons (PFCs) or hydrofluorocarbons (HFCs).

The concentration of CO2 for the historical period is based on the 20 year smoothed series from Law Dome ice cores as analysed by Etheridge *et al.* (2002) up to 1970 and

the values from IPCC 2001 report for 1980, 1990 and 2000. Annual values have been derived by cubic spline interpolation (through the software package xmgrace) (Fig. 1a).

The concentration of CH4 is also derived from Law Dome dataset (Etheridge *et al.*, 1998) using the global mixing ratios calculated from Antarctic and Greenland measurements which covers the years 1010-1890 at 10 year sampling interval with smoothing spline with 75 year cut off (Etheridge *et al.*, 1998, Table 2 part 1), and 1900-1992 with smoothing with 12.5 year cut-off (Etheridge *et al.*, 1998). The value for year 2000 from the IPCC report (1760 ppm) is introduced before applying a cubic spline interporlation to derive annual values (Fig. 1b).

The concentration of N2O is derived from the series of measurements in ice of Machida *et al.* (1995) and IPCC values for 1970, 1980, 1990 and 2000. Annual values are derived by cubic spline interpolation and 3 iterations of a 21 year moving average in order to remove short period oscillations (Fig. 1c)

The concentrations over the 21st century in the different SRES scenarios are taken directly from the tables given in annex II of the IPCC 2001 report.

The concentrations of CFCs are derived from the reconstructed histories of Walker *et al.* (2000). For the period 2000-2100 they are taken from the UNEP/WMO Scientific Assessment of Ozone Depletion (1998). The concentration for CFC-11 is replaced by an increased concentration (CFC-11*) that includes the radiative contribution of all other minor species of CFCS, PFCs and HCFCs included in the IPCC 2001 Annex II table II.2.10 and table II.2.4. The radiative forcing of all these halogenated compounds have been computed from the "WMO/UNEP Scientific Assessment of Ozone Depletion: 2002" table 1-6, page 1.32-1.33. The total of the radiative forcing of all these halogenated gases, except CFC-12 which is dealt with separately, has been converted back into the equivalent CFC-11 concentration (CFC-11*) that gives the same radiative forcing (Fig. 1d). Note that there is a small CFC-11* preindustrial concentration (12.48 pptv) that comes from the fact that there are natural sources of CF4 and evidence that the natural concentration of this gas is about 39 pptv (Harnish *et al.*, 1996). Annual values of CF4 and C2F6 have been derived using the aluminium production data (Weston, 1996). The role of the minor species increases in importance during the 21st century as can be seen by the increase of the equivalent CFC-11* which after reaching a first peak around 2000 due to the reduction of CFC-11 in application of the Montreal Protocol, starts to increase rapidly again in scenarios A2 and A1B.

3.2. The aerosol forcing

ARPEGE-Climat considers different kinds of aerosols: marine (due to emissions of sea salt), desert dust, black carbon and sulfates. Marine and desert aerosols, are held constant in all experiments and are defined according to Tanré *et al.* (1984). In an attempt to represent the variations of atmospheric black carbon (BC) concentrations due to fossil-fuel burning between 1860 and 2000, BC concentration data from Tanré *et al.* (1984) were scaled by the total fossil-fuel BC emissions estimated by Novakov *et al.* (2003) on the period 1875-2000. It was assumed that during the period 1860-

1875 black carbon emissions were at the same level as in 1875. The concentrations of sulfate aerosols are specified in all experiments from data provided for by Boucher and Pham (2002), see http://www-loa.univ-lille1.fr/~boucher/sres/ for more details. The direct effect of all aerosol types was taken into account, but no semi-direct or indirect effects were considered in this version of the model.

3.3. Experimental setup

3.3.1. The spin-up experiment

In order to get an initial state for the global coupled system, that represents a quasi-equilibrium of the climate system in preindustrial mode, a 70 year spin-up experiment was run. This experiment was initialized from climatological data for January 1st. The ocean and sea ice were initially at rest, the ocean three-dimensional salinity and temperature fields were taken from Levitus (1982). Sea ice concentration was also initialized from a climatology (Nomura and Grumbine, personal communication, 1995), while sea ice thickness in the Arctic and the Antarctic were respectively set equal to constant values of 3 and 1m. The concentrations of all atmospheric forcing agents were those of 1860 (see sections 3.2 and 3.3 and Fig. 1), considerered as representative of preindustrial conditions. The ocean salinity and temperature fields were relaxed toward Levitus climatology during the first 10 years of the spin-up, so that ocean dynamics should adopt a regime that is consistent with the three-dimensional climatologies. The model was run without any relaxation afterwards. During this spin-up experiment, sea ice and ocean reach a steady state after respectively about 15 and 30 years (except for deep circulation and the Antarctic Circumpolar Current).

3.3.2. The control experiment

Year 70 of the spin-up was chosen as an initial state for the preindustrial control experiment, as on the one hand it corresponds to a state of the modeled climate system well outside the initial drift and on the other hand it is not associated with an extreme variability pattern in terms of thermohaline circulation and global ocean surface temperature. Greenhouse gases and aerosols concentrations were held constant at 1860 values throughout the experiment. The experiment was run for 500 years.

3.3.3. The 1860-2000 historical experiment (20C3M)

The starting point of this experiment is year 110 of the preindustrial experiment. As this simulation spans the period 1860-2000, in the rest of this study it will be systematically compared to years 110-250 of the control experiment. The concentrations of forcing agents vary in time according to the estimates and observations presented in sections 3.2 and 3.3. This simulation is denoted as 20C3M throughout the rest of this study.

4. Model results

4.1. The preindustrial climate simulation

The climate simulated by CNRM-CM3 is colder compared to CNRM-CM2. However, at given forcing agents concentration levels the modeled climate drifts much less in terms of surface temperature, ocean temperature and salinity (see Table 3). This was one of the goals of the update of CNRM's global coupled model. Here no comprehensive validation of the preindustrial control climate is given, as the currently available reconstructions for this period, even if globally realistic, lack variability and are still rather uncertain in some regions.

Quantity	CNRM-CM2	CNRM-CM3
2m air global average temperature	+0.53 °C	-0.14 °C
Global average SST	+0.29 °C	-0.11 °C
Global average ocean temperature	+0.08 °C	-0.08 °C
Global average salinity	+0.092 psu	-0.025 psu

Table 3: drifts (per century) in CNRM-CM3 control experiment compared to CNRM-CM2.

The HadISST dataset (Rayner *et al.*, 2003) on the period 1871-1890 (even if assimilated observations are sparse in some places) is chosen as a validation dataset. The modeled global average SST is biased to the cold side (1.3°C). SST seems to be particularly underestimated in the tropics (2°C cold bias), especially in the Atlantic, were a very strong cold water upwelling occurs in the eastern part of the basin. Such an upwelling is also seen in tropical eastern Pacific. A perspective here might be to take the ocean surface current into account when computing the atmospheric stress over the ocean. As in these regions the surface current is not negligible, it would decrease the stress and reduce the intensity of upwellings.

The simulation of SST in the extratropics is better, with an non-significant positive bias of 0.3°C south of 30°S, and a negative bias of 1.2°C north of 30°N. Reasons for the reduced bias in the southern hemisphere are discussed in section 4.2.2. The thermohaline circulation (THC) index, computed as the maximum of Atlantic overturning streamfunction north of 30°N, reaches a steady state after 300 years of simulation. The modeled average value of 26.2 Sv during the last 200 years of the experiment is probably slightly too high, compared to current estimates (about 20 Sv). This is clearly a consequence of the too intense deep convection in the North Atlantic, particularly in Labrador Sea.

The average surface of the sea ice cover in the Arctic are respectively 12.4×10^6 km^2 (trend: $+0.4\times10^6$ km^2 per century) and 7.9×10^6 km^2 (trend -0.1×10^6 km^2 per century), to be compared with the values of 10 and 8×10^6 km^2 observed by satellite over the 1979-1987 period (Gloersen *et al.*, 1987).

Fig. 2 shows in global average (i) the difference between the incoming shortwave and outgoing longwave radiation at the top of the atmosphere (TOA), (ii) the net surface heat flux, (iii) the difference of the previous two and (iv) for a comparison the 2m air temperature (T_{2m}). All three residual fluxes are very small during the whole control

experiment, particularly (iii) which represents the imbalance in the atmospheric model (0.05 $W.m^{-2}$ in average).

4.2. Validation of present-day climatology

4.2.1. Atmosphere

It is apparent from Fig. 3, where global average modeled T_{2m} that the model is biased to the cold side. The difference between T_{2m} from the model and CRU2 climatology on land (Mitchell and Jones, 2005) is plotted on Fig. 4a, showing that during boreal winter the cold bias exceeds 3°C over most of the tropics and part of the northern high latitudes. In most of Canada, Central Asia and northeastern Siberia, in contrast, this bias is positive, exceeding 3°C in some places. These areas correspond to regions where the model underestimates the fraction of snow covering the ground. During boreal summer (Fig. 4b), the global bias is reduced, even if relatively strong biases persist in most of the tropics.

The modeled global average precipitations on land, at 2,5 mm/day is overestimated by about 20% on the 1971-2000 period. In tropical regions, during boreal winter, the model generally diagnoses too much rain in areas located to the south of the Equator (Fig. 5a), and conversely, in austral winter, it does so in areas lying north of the Equator (Fig. 5b), which indicates that modeled precipitations are too intense during the tropical rainy season. The main other contributions to the overall estimated precipitations are North America and northeastern Siberia during boreal summer. During boreal winter, the precipitations affecting central Europe and western Siberia seem to be due to intense perturbations penetrating too far east into these areas (the too zonal flow modeled by CNRM-CM3 in the North Atlantic is a reason for this), and causing strong precipitations also in western Europe.

4.2.2. Ocean

The general structure of the barotropic flow is correctly reproduced (see Fig. 6) . The maximum of the Gulf Stream and Kuroshio gyres, at respectively 53 and 46 Sv, are satisfactory when considering the relatively low spatial resolution of the model. For a comparison, the Gulf Stream transport was estimated to be 70 Sv (Schmitz and McCartney, 1993). Also, the Gulf Stream current does not leave the American coast before 40°N, which is too far north, but again this is a common bias among non eddy-resolving models. The subpolar gyre, at about –24 Sv, is correctly modelled. In contrast, the Antarctic Circumpolar Current, with an eastward transport of 81 Sv at Drake Passage, is weak compared to the best current estimates (130 ± 13 Sv, see Whitworth *et al.*, 1982). Conversely, the Atlantic Meridional Overturning Circulation (AMOC) index, defined here as the maximum of the overturning circulation north of 30°N, at nearly 25 Sv on the 1971-2000 period, is still rather intense.

The modeled global average sea surface salinity at 34.57 psu is close to the value of 34.64 psu suggested by Levitus data. The biases of modeled SST during the 1971-2000 period are less marked than biases on land surface temperature. With an average simulated SST of 17.4°C (compared to 18.3°C in HadISST for the period 1971-2000),

the bias is still of –0.9°C. In most areas, the bias on modeled SST is negative (between 1 and 2°C), except in the Arctic, and the 50°S-20°S latitude band in the Pacific and Indian ocean sectors, where they are close to observations (see Fig. 7). Two warm SSTs appear near the western coasts of South and North America and the southwestern coasts of Africa, which are due to the fact the frequently observed stratocumulus in these areas are not reproduced by CNRM-CM3. The strongest positive SST bias occurs near the Antarctic and as far north as 50°S. The first reason for this is that the ocean component assumes isopycnal heat diffusion, and in the case of the vertically well-mixed Antarctic waters, too much heat is diffused toward the surface, in addition to the contribution of vertical heat diffusion. The second reason is due to the too transparent modeled clouds in this area, which lead to an overestimate of the shortwave radiation reaching the surface during austral summer.

4.2.3. Sea ice

The modeled sea ice cover is realistic in surface and extension in both hemispheres. However in the Arctic it is probably too thin (1.53 m yearly average during 1971-2000) as well as in the central Arctic (1.79 m). Ice thickness data from submarine cruises in the Central Arctic on the periods 1958-1976 and 1993-1997, analysed by Rothrock *et al.* (1999) respectively give values of 3.1 and 1.8 m, while CNRM-CM3 diagnoses 1.99 and 1.63 m. Another bias of the model is due to the generally too zonal atmospheric stress over sea ice along Siberian coasts, but also to the lack of strait opening between the islands located north of Siberia and the continent. Sea ice drifts zonally in the Seas of Chukchi and Kara, as well as east of Franz-Joseph Land, forms ridges and hence accumulates near the eastern shores of the islands, reaching overestimated thicknesses. The modeled ice edge is satisfactory in the North Atlantic (see Figs. 8a and 8c), even if there is too much ice in the Barents Sea, and a slight lack of sea ice in the Labrador Sea. In contrast, due the bad position of the Aleutian Low in the model, sea ice tends to drift too extensively in the Sea of Okhotsk during the winter, as shown by Fig. 8a. The volume and surface of ice transported through Fram Strait, at 0.69×10^6 km^2.yr^{-1} and 1340 km^3.yr^{-1} respectively, are underestimated, as observational data by Vinje (2000) yield values of 1.1×10^6 km^2.yr^{-1} and 2900 km^3.yr^{-1} respectively. This is mainly due to the fact ice crossing Fram Strait is too thin, but the underestimated southward sea ice velocity component in this region also plays a role.

In the Antarctic (see Figs. 8b and 8d), the annual cycle of the sea ice cover is slightly too marked, with an average minimum of 0.2×10^6 km^2 in March and a maximum of 17.4×10^6 km^2 in September, and the 1971-2000 average modeled thickness is also underestimated there (0.33 m). Top and bottom sea ice ablation are overestimated in the model, due to the too strong ocean heat flux and net surface shortwave irradiance, which causes a quasi-total melting of sea ice during the austral summer. During the winter, the only small biais is observed to the north of Ross Sea, at about 65°S, where there is a lack of sea ice. This is due to the too zonal ocean flow there, itself a consequence of the non-representation of an undersurface mountain that deflects the flow in the real world.

4.3. Validation of climate variability

4.3.1. ENSO, NAO and PDO

The Niño3 index anomalies (average SST computed over the domain 150°W-90°W, 5°S-5°N) is plotted in Fig. 9. Compared to HadISST observations, the modeled index exhibits overestimated interannual variability and too large temperature differences between warm and cold phases of ENSO (El Niño Southern Oscillation). A frequency spectrum of the index (not shown) indicates that ENSO modeled by CNRM-CM3 is too regular, with a dominant frequency of two to three years, whereas observations suggest does that dominant frequencies span a broader spectrum (2 to 7 years). The observed (HadISST) and modeled time-correlation of Niño3 index with SST is plotted in Fig. 10. A comparison with observations shows that teleconnections of SST with ENSO are realistic, except in the northwestern Pacific, where SST should be dominated by the PNA (Pacific North American) and not by ENSO. The teleconnection between SST in the northern Indian Ocean with ENSO is also a model artefact.

Fig. 11 shows the mean NAO anomalies computed from sea level pressure modeled by CNRM-CM3. The variability of the modeled and observed indices are comparable. A prominent feature of the observed NAO index is its upward trend from the 1970, which is not reproduced by the 20C3M simulation, even during its stabilization phase (2000-2100) with forcing agents held constant at 2000 values. The climate change experiments also presented in Fig. 11 do not show any marked trend for this index either. However there is currently no agreement in the community about the possible link between global warming and an increase of the NAO index, as Rind (1998) concluded there should be more NAO positive phases in a warmer climate, whereas Shindell *et al.*(1998) found such a link existed in the GISS model only with full stratosphere.

4.3.2. Coupled THC variability in the North Atlantic

The THC index was correlated with the yearly average convection depth in Greeland-Iceland-Norwegian Seas (GIN Seas) and in Labrador Sea at lags ranging from –20 to +20 years (THC leads if the lag is positive, see Fig. 12). The maximum correlation with GIN Seas convection depth occurs as convection leads by 4 years, but is much smaller than with Labrador Sea mixed layer depth (THC lags 2 years). This shows that in the model, the entrainment of the Atlantic Meridional Overturning Circulation (AMOC) is mostly due to convection in the Labrador Sea, probably due to the much less intense modeled winter mixed layer depth in the GIN Seas.
The potential predictability (from ocean circulation patterns) of the spatially averaged SST in the 50°W-10°W / 40°N-60°N box, shown by Latif *et al.* (2004) is also verified in the model, as its maximum correlation with the THC index (nearly 0.40) occurs as the THC index leads by 2 years (Fig. 12).

4.3.3. Temperature extremes

Preliminary analyses of extremes were carried out in the 20C3M experiment. The yearly average number of freezing days n_{fd}^{g} calculated from CRU TS 2.1 (Mitchell

and Jones, 2005) and from the 20C3M simulation are compared in Fig. 13. As already pointed out, the simulation has a global cold bias, and, as expected, the modeled n_{fd}^{g} is larger than observed. However, even in the context of the warmer climates simulated in the 21st century scenario experiments, the modelled decrease in n_{fd}^{g} is not as steep as observed in the recent period.
The summer heat wave duration index in Northern America is plotted in Fig. 14. It is defined as the maximum number of consecutive days for which the maximum temperature exceeds the normal maximum temperature (calculated over 1961-1990) by at least 5K (Haylock, 2003). As the modelled summer T_{2m} in this region is realistic in terms of probability distribution function and average, the match between the heat wave index computed from 20C3M and the observations is a rather good. The change in index trend is even reproduced around the 1970s. This is also the case for intense precipitations in the same region, defined as the annual number of days for which rainfall exceeds 10 mm (Fig. 15), even though the annual cycle of this variable, in North America, is not correctly modelled. North America observation indices were computed from a daily dataset of temperature and precipitations covering the North American continent, constructed on the same basis as the western USA dataset from Eischeid *et al.*(2000).

4.4. 20th century modeled climate change

4.4.1. Atmosphere

The global warming simulated by 20C3M during the 20th whole century, close to 1°C, is overestimed compared to observations (0.7°C, Jones and Moberg, 2003). Moreover, it is overestimated in the tropics and too slow in the polar regions. The fact that the indirect effect of sulfate aerosols, which causes cooling surface cooling, is not included in the model, may explain the too intense modeled global warming, but not its erroneous spatial repartition. In a sensitivity experiment with IPSL-CM4 coupled system (Marti *et al*., 2005), Dufresne *et al*. (2005), estimate the cooling caused by the sulfate aerosols of anthropogenic origin is close to 0.5°C over the period 1860-2000, which suggests that considering their indirect effect in CNRM-CM3 would probably reduce the modeled warming. IPSL-CM4 (Marti *et al.*, 2005), uses an ocean-component which is very similar to the one included in CNRM-CM3, and the two coupled models share the same radiative code (Marti *et al.*, 2005).

Fig. 3 shows the mid-20th century warming was not captured by the model. There may be at least two reasons for this. The first reason is that this warming concerned mostly the Arctic and was probably due to a particular phase of the NAO, and no outstanding NAO event happened at that particular time in the model (see Fig. 11). This is not surprising, as observations a priori represent one particular realization of climate variability over the 20th century. The second reason is that the mid-20th century warming may have been partly due to solar variability, and the solar constant did not vary in 20C3M. However, another simulation, run with CNRM-CM3 in the same conditions as 20C3M, but with solar variability and volcanic forcing, did not show any pronounced mid-20th century warming.

Global precipitations rise from a global average of 3.02 mm/day to 3,08 mm/day over the 20th century, whereas the control does not show any trend during the part of the run this period should be compared to. If the global average amount of precipitations is clearly overestimated, it is rather difficult to compare the modeled trend to an observed trend, as the latter is still uncertain.

4.4.2. Ocean

The modeled surface global warming of the ocean during the 20th century is close to the atmospheric surface warming and approaches 0.9°C, without any stabilization between 1940 and 1980 (see Fig. 16). This is consistent with the modeled T2m variations over the same period. Another good oceanic indicator of climate change is sea level rise (with contributions of continental ice melting and of oceanic thermal expansion). Here, only the thermal effect was estimated (see Fig. 16), and at 0.06 m between 1901 and 2000 ,it is close to current estimates (Gregory *et al.*, 2001).
The THC index follows a linearly decreasing trend of -0.26 Sv/decade. As pointed out in section 4.3.2., in CNRM-CM3 it is quite strongly linked with the intensity of ocean convection in Labrador Sea. Since the latter decreases during the 20th century in 20C3M, due to the warming of the Labrador Sea area, making surface waters less prone to convective sinking, the modeled trend on the THC index is not surprising.
Global salinity does not show any trend over the 20th century. It is close to observations (34,57 psu, obs. Levitus 34,64 psu).

4.4.3. Sea ice

The modeled year-average surface of the arctic sea ice cover is stable during the first 60 years of the 20th century (11.8×10^6 km^2), then it loses 0.8×10^6 km^2 over the 1960-2000 period, which compares favourably with analyses of satellite observations from NSIDC (Boulder, USA) estimating arctic sea ice depletion to 0.85×10^6 km^2 between 1978 and 2002. In the Antarctic, the modeled sea ice cover and observations do not show any significant trend, but the coupled system produces marked multi-decadal variability. For example a polynia is generally present in the Weddell Sea between 1950 and the beginning of the 1970s. This aspect of the 20C3M simulation will be studied in a forthcoming paper.

5. Conclusion

CNRM-CM3 was used recently to perform a total of more than 2000 years of simulations, that are currently analysed in preparation for the IPCC fourth assessment report. These experiments include a preindustrial control, a 20C3M simulation, 21st century scenarios and stabilisations for the 22nd and 23rd centuries, 1% increase per year of the atmospheric concentration of CO_2 to doubling, quadrupling (from preindustrial level) and stabilisations at 2x and 4xCO_2. In the preindustrial control experiment, the model drift is limited to about -0.1°C per century in SST and T_{2m}, but this version is biased to the cold side, and the global simulated surface warming is overestimated in the 20C3M simulation. Consistently with the cold drift, the volume and surface of sea ice (particularly in the Arctic), even if realistic, show a positive

trend. The average climate of the end of the 20th century is globally correctly simulated, but is still cold in many aspects. Despite the cold bias of CNRM-CM3 model, it is capable of simulating many aspects of natural variability, a few of them being addressed in this study.

Further developments of the model will be focused on reducing the negative bias of CNRM-CM3. Introducing more physically-based parameterisations to describe atmospheric turbulence in stable cases could represent a way to improve the model. Taking the surface ocean current in atmosphere-ocean stress computations will also contribute to reduce oceanic upwellings near the western coasts of South America and Africa, hence reducing the SST cold biais in these areas. Another research theme that will be addressed is about the aerosols and their interactions with clouds and precipitations, particularly through the indirect effects of sulfate aerosols. These effects will contribute to a slight cooling of the modeled climate, but taking them into account should reduce the modeled 20th century global warming.

Acknowlegments
Support by a grant from the European Commission's 6th Framework Programme (ENSEMBLES, contract GOCE-CT-2003-505539) is gratefully acknowledged.

References

Ashrit RG, Douville H, Rupa Kumar K (2003) Response of the Indian Monsoon and ENSO-monsoon teleconnection to enhanced greenhouse effect in transient simulations of the CNRM coupled model. J Meteorol Soc Japan 81: 779-803

Barthelet P, Terray L, Valcke S (1998) Transient CO2 experiment using the ARPEGE/OPAICE non flux corrected coupled model. Geophysical Research Letters 25: 2277-2280

Bitz, C. M., M. Holland, M. Eby and A. J. Weaver, 2001: Simulating the ice-thickness distribution in a coupled climate model. J. Geophys. Res., 106, 2441-2463.

Blanke, B. and Delecluse, P. (1993): Variability of the tropical Atlantic Ocean simulated with a general circulation model with two different mixed layer physics. J. Phys. Oceanogr., 23, 1363-1388

Bossuet, C., Déqué, M. and Cariolle, D. (1998) : Impact of a simple parameterization of convective gravity-wave drag in a stratosphere-troposphere general circulation model and its sensitivity to vertical resolution. Ann. Geophys. 16, 238-249.

Bougeault, P. (1985): A simple parameterization of the large-scale effects of cumulus convection, Mon. Wea. Rev. 113, 2108-2121

Camberlin P, Chauvin F, Douville H, Zhao Y (2004) Simulated ENSO-tropical rainfall teleconnections in present-day and under enhanced greenhouse gases conditions. Climate Dyn 23: 641-657

Cariolle, D. and Déqué, M. (1986): Southern hemisphere medium-scale waves and total ozone disturbances in a spectral general circulation model. J Geophys. Res 91, 10825-10846

Cariolle, D., Lasserre-Bigory, A., Royer, J.-F. and Geleyn, J.-F. (1990): A general circulation model simulation of the springtime Antarctic ozone decrease and its impact on mid-latitudes, J. Geophys. Res. Atmos. 95, 1883-1898

Chapelon, N., Douville, H., Kosuth, P. and Oki, T. (2002): Off-line simulation of the Amazon water balance: a sensitivity study with implications for GSWP, Clim. Dyn., 19, 141-154

Chauvin F, Royer JF, Douville H (2005) Interannual variability and predictability of African easterly waves in a GCM. Climate Dyn 24: 523-544

Covey C, Abe Ouchi A, Boer GJ, Boville BA, Cubasch U, Fairhead L, Flato GM, Gordon H, Guilyardi E, Jiang X, Johns TC, Le Treut H, Madec G, Meehl GA, Miller R, Noda A, Power SB, Roeckner E, Russell G, Schneider EK, Stouffer RJ, Terray L, von Storch JS (2000) The seasonal cycle in coupled ocean-atmosphere general circulation models. Climate Dyn 16: 775-787

Davey MK, Huddleston M, Sperber KR, Braconnot P, Bryan F, Chen D, Colman RA, Cooper C, Cubasch U, Delecluse P, De Witt D, Fairhead L, Flato G, Gordon C, Hogan T, Ji M, Kimoto M, Kitoh A, Knutson TR, Latif M, Le Treut H, Li T, Manabe S, Mechoso CR, Meehl GA, Power SB, Roeckner E, Terray L, Vintzileos A, Voss R, Wang B, Washington WM, Yoshikawa I, Yu JY, Yukimoto S, Zebiak SE (2002) STOIC: A study of coupled model climatology and variability in tropical ocean regions. Climate Dyn 18: 403-420

Déqué M., Dreveton, C., Braun, A., and Cariolle, D. (1994): The ARPEGE/IFS atmosphere model : A contribution to the French community climate modelling. Climate Dyn., 10, 249-266.

Déqué, M. and J.P. Piedelievre (1995): High resolution climate simulation over Europe. Climate Dyn., 11, 321-339.

Déqué, M., Marquet, M. and Jones, R.G. (1998) : Simulation of climate change over Europe using a global variable resolution general circulation model. Clim. Dynam. 14, 173-189.

Déqué, M., Braun, A., Piedelievre, J.-P., Marquet, P., Dandin, P., Guérémy, J.-F., Geleyn, J.-F., Bazile, E., Piriou, J.-M., Yessad, K., Courtier, P. and Rochas, P. (1999): ARPEGE version 3, documentation algorithmique et mode d'emploi (in French, available from CNRM/GMGEC, Météo-France, 42 avenue G. Coriolis, 31057 Toulouse, France)

Doblas-Reyes FJ, Déqué M, Valero F, Stephenson DB (1998) North Atlantic wintertime intraseasonal variability and its sensitivity to GCM horizontal resolution. Tellus (Ser A) 50: 573-595

Douville, H., Royer, J.-F. and Mahfouf, J.-F. (1995a): A new snow parametrization for the Météo-France climate model. Part I: Validation in stand-alone experiments, Clim. Dyn. 12, 21-35

Douville, H., Royer, J.-F. and Mahfouf, J.-F. (1995b): A new snow parametrization for the Météo-France climate model. Part II: Validation in a 3-D GCM experiments, Clim. Dyn. 12, 37-52

Douville, H. (2002) Influence of soil moisture on the Asian and African monsoons. Part II: Interannual variability. J Climate 15: 701-720

Douville, H., Chauvin F, Planton S, Royer JF, Salas y Mélia D, Tyteca S (2002) Sensitivity of the hydrological cycle to increasing amounts of greenhouse gases and aerosols. Climate Dyn 20: 45-68

Douville, H. (2003) Assessing the influence of soil moisture on seasonal climate variability with AGCMs. J Hydrometeor 4: 1044-1066

Douville, H. (2004) Relevance of soil moisture for seasonal atmospheric predictions: Is it an initial value problem? Climate Dyn 22: 429-446

Douville, H. (2005): Limitations of time-slice experiments for predicting regional climate change over South Asia. Climate Dynamics, 24, 373-391, DOI: 10.1007/s00382-004-0509-7

Dufresne, J.-L., J. Quaas, O. Boucher, S. Denvil and L. Fairhead (2005) : Contrasts in the effects on climate of anthropogenic sulfate aerosols between the 20th and the 21st century. Accepted for publication in Geophys. Res. Lett.

Eischeid, J.K., P.A. Pasteris, H.F. Diaz, M.S. Plantico and N.J. Lott (2000): Creating a serially complete, national daily time series of temperature and precipitation for the western United States. J. Appl. Meteorol., 39, 1580-1591.

Etheridge, D.M., *et al.*, 2002, Ice Core, Firn Air and Archived Air Atmospheric Methane Concentration Data, IGBP PAGES/World Data Center for Paleoclimatology Data Contribution Series #2002-039. NOAA/NGDC Paleoclimatology Program, Boulder CO, USA.

Etheridge, D. M., Steele, L. P., Francey, R. J., and Langenfelds, R. L., 1998, Atmospheric methane between 1000 A.D. and present: Evidence of anthropogenic emissions and climatic variability J. Geophys. Res. Vol. 103, No. D13, p. 15,979 (98JD00923)

Frankignoul C, Kestenare E, Botzet M, Carril AF, Drange H, Pardaens A, Terray L, Sutton R (2004) An intercomparison between the surface heat flux feedback in five coupled models, COADS and the NCEP reanalysis. Climate Dyn 22: 373-388

Gates WL, Boyle JS, Covey C, Dease CG, Doutriaux CM, Drach RS, Fiorino M, Gleckler PJ, Hnilo JJ, Marlais SM, Phillips TJ, Potter GL, Santer BD, Sperber KR, Taylor KE, Williams DN (1999) An overview of the results of the Atmospheric Model Intercomparison Project (AMIP I). Bull Amer Meteorol Soc 80: 29-55

Gibelin, A.L. and Déqué, M. (2003): Anthropogenic climate change over the Mediterranean region simulated by a global variable resolution model. Climate Dynamics, 20: 327-339.

Gloersen P., Campbell W.J., Cavalieri D.J., Comiso J.C., Parkinson C.L. et Zwally H.J., 1992, Arctic and Antarctic sea ice, 1978-1987: satellite passive microwave observations and analysis. NASA Spec. Publ., NASA SP-511, 290 pp.

Gregory, J.M., J. A. Church, G. J. Boer, K. W. Dixon, G. M. Flato, D. R. Jackett, J. A. Lowe, S. P. O'Farrell, E. Roeckner, G. L. Russell, R. J. Stouffer, M. Winton (2001): Comparison of results from several AOGCMs for global and regional sea-level change 1900-2100. Clim. Dyn. 18, 225-240.

Guérémy JF, Déqué M, Braun A, Piedelievre JP (2005) Actual and potential skill of seasonal predictions using the CNRM contribution to DEMETER: Coupled versus uncoupled model. Tellus (Ser A) 57: 308-319

Guilyardi E, Madec G, Terray L (2001) The role of lateral ocean physics in the upper ocean thermal balance of a coupled ocean-atmosphere GCM. Climate Dyn 17: 589-599

Hagemann S, Machenhauer B, Jones R, Christensen OB, Déqué M, Jacob D, Vidale PL (2004) Evaluation of water and energy budgets in regional climate models applied over Europe. Climate Dyn 23: 547-567

Harnish J, R Borchers, P. Fabian, H.W. Gäggeler, U. Schotterer, 1996: Effect of natural tetrafluoromethane, Nature 384, 32.

Haylock, M., 2003: STARDEX diagnostic extremes indices software: User information. Version 3.2.6, May 2003. Available from the STARDEX web-site: http://www.cru.uea.ac.uk/projects/stardex/

Hunke, E. C. and Dukowicz, J. K. (1997): An elastic-viscous-plastic model for sea ice dynamics. J. Phys. Oceanogr., 27, 1849-1867

Hunke, E. C. and Lipscomb, W. H. (2002): CICE: the Los Alamos sea ice model, documentation and software User's Manual. T-3 Fluid Dynamics Group, Los Alamos National Laboratory, Tech. Rep. LACC-98-16 v.3.

Jia Y (2003) Ocean heat transport and its relationship to ocean circulation in the CMIP coupled models. Climate Dyn 20: 153-174

Jones, P.D. and Moberg, A. (2003): Hemispheric and large-scale surface air temperature variations: An extensive revision and an update to 2001. Journal of Climate, 16, 206-223.

Joussaume S, Taylor KE, Braconnot P, Mitchell JFB, Kutzbach JE, Harrison SP, Prentice IC, Broccoli AJ, Abe-Ouchi A, Bartlein PJ, Bonfils C, Dong B, Guiot J, Herterich K, Hewitt CD, Jolly D, Kim JW, Kislov A, Kitoh A, Loutre MF, Masson V, McAvaney B, McFarlane N, Denoblet N, Peltier WR, Peterschmitt JY, Pollard D, Rind D, Royer JF, Schlesinger ME, Syktus J, Thompson S, Valdes P, Vettoretti G, Webb RS, Wyputta U (1999) Monsoon changes for 6000 years ago: Results of 18 simulations from the Paleoclimate Modeling Intercomparison Project (PMIP). Geophysical Research Letters 26: 859-862

Lambert SJ, Boer GJ (2001) CMIP1 evaluation and intercomparison of coupled climate models. Climate Dyn 17: 83-106

Latif, M., E. Roeckner, M. Botzet, M. Esch, H. Haak, S. Hagemann, J. Jungclaus, S. Legutke, S. Marsland and U. Mikolajewicz (2004): Reconstructing, monitoring and predicting multidecadal-scale changes in the North Atlantic thermohaline circulation with sea surface temperature. J. Climate 17, 1605-1613.

Levitus, S., 1982: Climatological Atlas of the World Ocean, NOAA Professional Paper 13. US Dept of Commerce: National Oceanic and Atmospheric Administration.

Lorant V, Royer JF (2001) Sensitivity of equatorial convection to horizontal resolution in aqua-planet simulations with a variable-resolution GCM. Mon Weather Rev 129: 2730-2745

Louis, J.F., M. Tiedtke, and J.F. Geleyn, 1982: A short history of the operational PBL parameterization at ECMWF. Proceedings of the Workshop on Planetary Boundary Parameterization, European Centre for Medium-Range Weather Forecasts, Shinfield Park, Reading RG2 9AX, UK, pp. 59-79.

Machida, T., T. Nakazawa, Y. Fujii, S. Aoki and O. Watanabe, 1995: Increase in the atmospheric nitrous oxide concentration during the last 250 years. Geophysical Research Letters, 22, 2921-2924.

Madec, G. and Imbard, M. (1996): A global ocean mesh to overcome the North Pole singularity, Clim. Dyn. 12, 381-388

Madec G., Delecluse P., Imbard M., Lévy C. (1998): OPA version 8.1 Ocean General Circulation Model Reference Manual, Notes du Pôle de Modélisation, Institut Pierre-Simon Laplace, n°11, 91 pp [Available from Laboratoire d'Océanographie Dynamique et de Climatologie, Université Paris VI, Paris 75252, France.]

Mahfouf, J.-F., A. Manzi, J. Noilhan, H. Giordani, and M. Déqué (1995): The land surface scheme ISBA within the Météo-France climate model ARPEGE. Part I: Implementation and preliminary results. J. Climate, 8, 2039-2057.

Mahfouf, J.-F. and Noihan, J. (1996): Inclusion of a gravitational drainage in a land surface scheme based on the force-restore method. J. Appl. Meteorol., 35, 987-992

Marti, O., P. Braconnot, J. Bellier, R. Benshila, S. Bony, P. Brockmann, P. Cadule, A. Caubel, S. Denvil, J.-L. Dufresne, L. Fairhead, M.-A. Filiberti, M.-A. Foujols, T. Fichefet, P. Friedlingstein, J.-Y. Grandpeix, F. Hourdin, G. Krinner, C. Lévy, G. Madec, I. Musat, N. de Noblet, J. Polcher and C. Talandier (2005): The new IPSL climate system model: IPSL-CM4, Tech. Report., Institut Pierre Simon Laplace, Paris, France. http://igcmg.ipsl.jussieu.fr/Doc/IPSLCM4

Mascart P., Noilhan, J. and Giordani, H. (1995): A modified parameterization of flux profile relationships in the surface layer using different roughness length values for heat and momentum. Bound. Layer Met. 72, 331-344

Masson V, Champeaux J-L, Chauvin F, Meriguet C, Lacaze R (2003) A global database of land surface parameters at 1-km resolution in meteorological and climate models. J Climate 16: 1261-1282

Maynard K, Royer JF (2004a) Effects of "realistic" land-cover change on a greenhouse-warmed African climate. Climate Dyn 22: 343-358

Maynard K, Royer JF (2004b) Sensitivity of a general circulation model to land surface parameters in African tropical deforestation experiments. Climate Dyn 22: 555-572

Maynard K, Royer JF, Chauvin F (2002) Impact of greenhouse warming on the West African summer monsoon. Climate Dyn 19: 499-514

Meehl GA, Boer GJ, Covey C, Latif M, Stouffer RJ (2000) The Coupled Model Intercomparison Project (CMIP). Bull Amer Meteorol Soc 81: 313-318

Mitchell, T.D. and P.D. Jones, 2005: An improved method of constructing a database of monthly climate observations and associated high-resolution grids. International Journal of Climatology, vol 25, 693-712.

Morcrette, J.-J. (1990): Impact of changes to the radiation transfer parameterizations plus cloud optical properties in the ECMWF model. Mon. Wea. Rev., 118, 847-873

Morcrette, J.-J. (1991): Radiation and cloud radiative properties in the European Centre for Medium Range Forecasts forecasting system, J. Geophys. Res. 95, 9121-9132

Moustaoui M, Royer JF, Chauvin F (2002) African easterly wave activity in a variable resolution GCM. Climate Dyn 19: 289-301

Noilhan, J. and Planton, S. (1989): A simple parameterization of land surface processes for meteorological models, Mon. Wea. Rev. 117, 536-549.

Novakov, T., V. Ramanathan, J.E. Hansen, T.W. Kirchstetter, M. Sato, J.E. Sinton, and J.A. Satahye 2003. Large historical changes of fossil-fuel black carbon aerosols. Geophys. Res. Lett. 30, no. 6, 1324, doi:10.1029/2002GL016345.

Oki, T. and Sud, Y.C. (1998): Design of Total Runoff Integrating Pathways (TRIP) A global river channel network. Earth Interactions, vol.2, paper 1.

Oki, T., Wishimyra, T., Dirmeyer, P. (1999): Assessment of annual runoff from land surface models using Total Runoff Integrating Pathways (TRIP). J. Meteorol. Soc. Japan 77, 235-255.

Palmer TN, Alessandri A, Andersen U, Cantelaube P, Davey M, Delecluse P, Deque M, Diez E, Doblas-Reyes FJ, Feddersen H, Graham R, Gualdi S, Guérémy JF, Hagedorn R, Hoshen M, Keenlyside N, Latif M, Lazar A, Maisonnave E, Marletto V, Morse AP, Orfila B, Rogel P, Terres JM, Thomson MC (2004) Development of a European multimodel ensemble system for seasonal-to-interannual prediction (DEMETER). Bull Amer Meteorol Soc 85: 853-872,805

Paulson, C.A. and Simpson, J.J. (1977): Irradiance measurements in the upper ocean. J. Phys. Oceanogr., 7, 952-956.

Pontaud M, Céron J-P, Kimoto M, Pluviaud F, Terray L, Vintzileos A (2000) CoPIVEP: a theory-based analysis of coupled processes and interannual variability in the Equatorial Pacific in four coupled GCMs. Climate Dyn 16: 917-934

Rayner, N.A., Parker, D.E., Horton, E.B., Folland, C.K., Alexander, L.V., Rowell, D.P., Kent, E.C. and Kaplan, A. (2003) Global analyses of sea surface temperature,

sea ice, and night marine air temperature since the late Nineteenth Century. Journal of Geophysical Research, 108 (D14), 4407, doi: 1029/2002JD002670

Ricard, J.-L. and Royer, J.-F. (1993): A statistical cloud scheme for use in a AGCM, Ann. Geophysicae 11, 1095-1115.

Rind, D. (1998): Latitudinal temperature gradient and climate change. J. Geophys. Res., 103, 5943-5971.

Rothrock, D.D., Y.Yu, and G.A. Maykut (1999): Thinning of the arctic sea ice cover. Geophys. Res. Letters, vol.26, p.3469-3472.

Royer, J.-F., D. Cariolle, F. Chauvin, M. Déqué, H. Douville, R.M. Hu, S. Planton, A. Rascol, J.-L. Ricard, D. Salas y Mélia, F. Sevault, P. Simon, S. Somot, S. Tytéca, L. Terray, S. Valcke (2002): Simulation des changements climatiques au cours du 21ème siècle incluant l'ozone stratosphérique. C. R. Geophys., 334, 147-154.

Salas-Mélia, D. (2002): A global coupled sea ice-ocean model. Ocean Modelling 4, 137-172

Schmitz, W., and M. McCartney (1993): On the North Atlantic circulation. Rev. Geophys., 31, 29-49.

Shindell, D., R. Miller, G. Schmidt and L. Pandolfo (1999): Simulation of recent northern winter climate trends by greenhouse-gas forcing. Nature, 399, 452-455.

Tanré, D., Geleyn, J.-F. and Slingo, J. M. (1984): First results of the introduction of an advanced aerosol-radiation interaction in the ECMWF low resolution global model. In Aerosols and Their Climatic Effects. H.E. Gerber and A. Deepak, Eds., A. Deepak Publ., Hampton, Va., 133-177

Terray L, Thual O, Belamari S, Déqué M, Dandin P, Delecluse P, Lévy C (1995) Climatology and interannual variability simulated by the ARPEGE-OPA coupled model. Climate Dyn 11: 487-505

Terray, L., Valcke, S. and Piacentini, A. (1998): OASIS 2.2 User's Guide and Reference Manual, TR/CMGC/98-05 [Available from CERFACS, 42 ave. G. Coriolis, 31057 Toulouse, France.]

Terray, L., Demory, M.-E., Déqué, M., de Coetlogon, G. and Maisonnave, E. (2004): Simulation of late-twenty-first-Century changes in wintertime atmospheric circulation over Europe due to anthropogenic causes. J. of Clim., 17, No.34, 4630-4635.

Thorndike, A. S., D. A. Rothrock, G. A. Maykut and R. Colony (1975): The thickness distribution of sea ice. J. Geophys. Res., 80, 4501-4513.

UNEP/WMO Scientific Assessment of Ozone Depletion: 1998 Chapter 11: Halocarbon scenarios for the future ozone layer and related consequences, Guus Velders (RIVM) and Sasha Madronich (NCAR), Version 5, June 3, 1998,

Voldoire A, Royer JF (2004) Tropical deforestation and climate variability. Climate Dyn 22: 857-874

Voldoire A, Royer JF (2005) Climate sensitivity to tropical land surface changes with coupled versus prescribed SSTs. Climate Dyn 24: 843-862.

Walker, S. J., R. F. Weiss and P. K. Salameh, Reconstructed histories of the annual mean atmospheric mole fractions for the halocarbons CFC-11, CFC-12, CFC-113 and carbon tetrachloride. Journal of Geophysical Research, 105, C6, 14,285-14,296, 2000

Weston R.E., 1996: Possible greenhouse effects of tetrafluoromethane and carbon dioxide emitted from aluminum production. Atmos Env 30, 2901-2910

Whitworth, T., W. D. Nowlin, and S. J. Worley, 1982: The net transport of the Antarctic Circumpolar Current through Drake Passage. J. Phys. Oceanogr., 12, 960-971.

Zeng, X., 2001: Global vegetation root distribution for land modeling.

WMO/UNEP Scientific Assessment of Ozone Depletion: 2002 (http://www.wmo.ch/web/arep/reports/o3_assess_rep_2002_front_page.html)

Figures

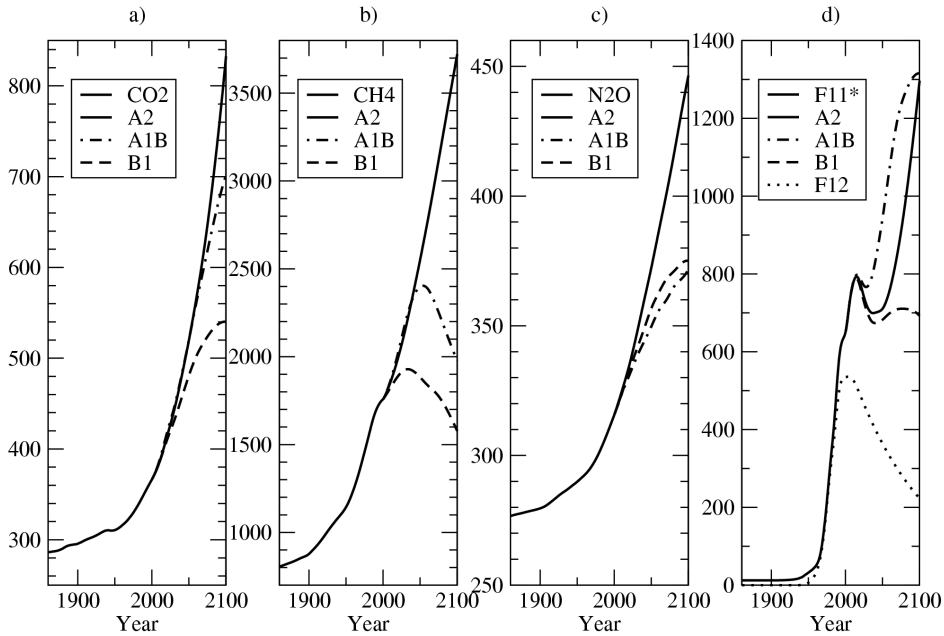

Figure 1: Greenhouse gases concentrations used for the historical experiments (preindustrial control, 20C3M experiment) and for the scenario experiments (21st century); (a) CO2 ; (b) CH4 ; (c) N2O ; (d) F11* represents CFC-11 plus all the other minor species of CFCs, PFCs and HCFCs

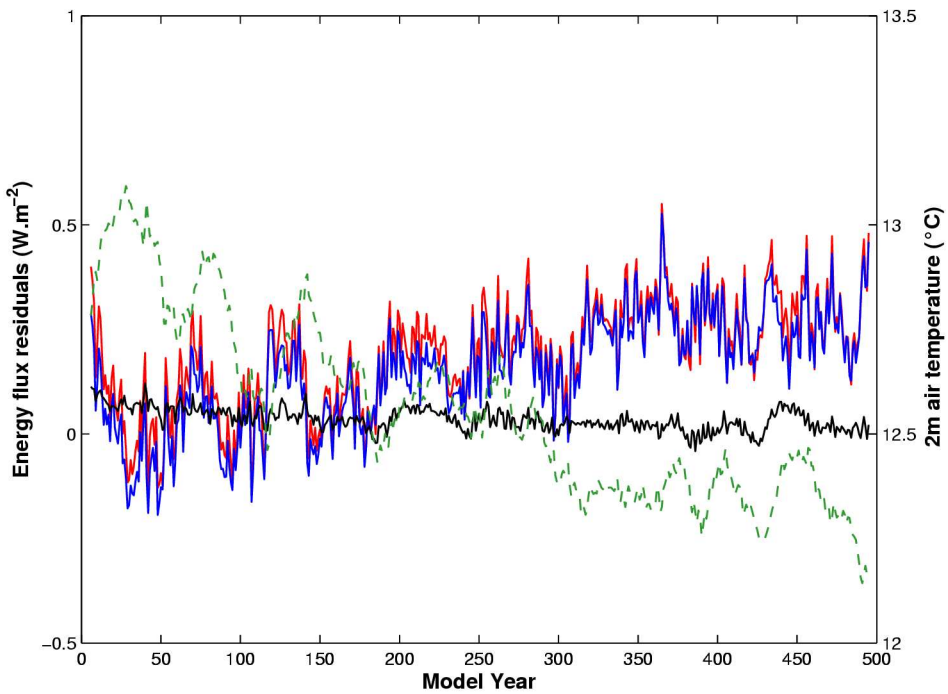

Figure 2: Control experiment: top of atmosphere residual flux (integrated incoming shortwave minus outgoing longwave radiation), surface residual flux (integrated net heat flux), difference of the previous two (respectively plotted in red, blue and black). Global average T_{2m} is plotted in green.

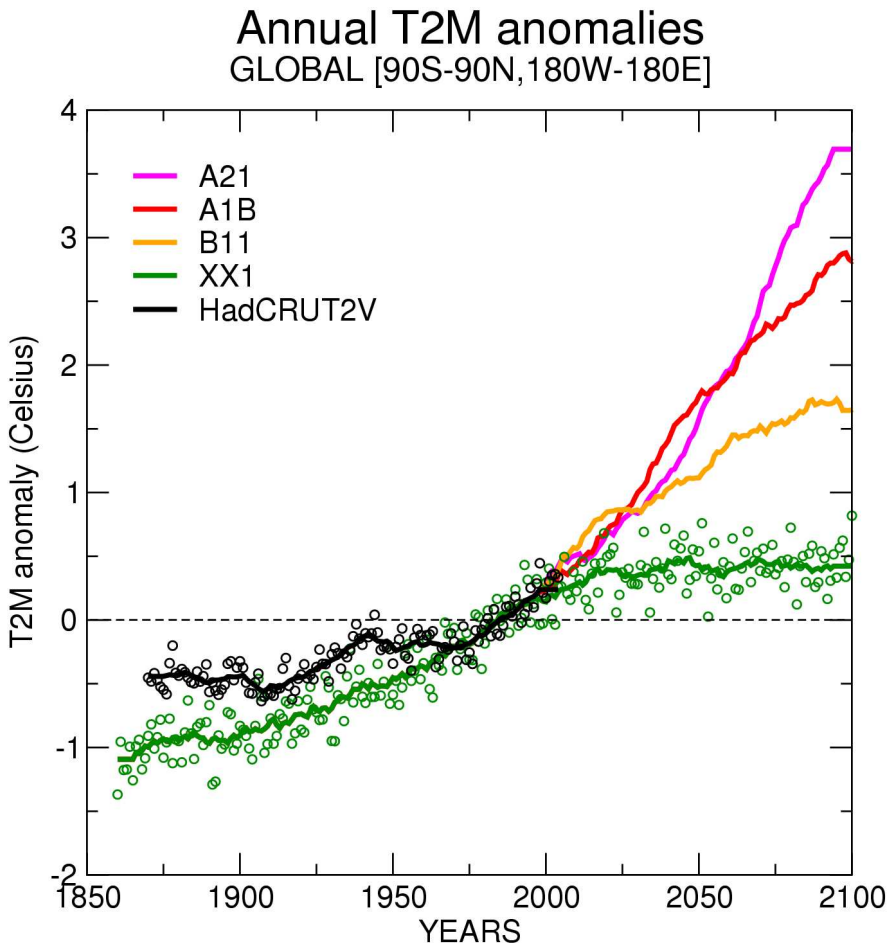

Figure 3: Global average T_{2m} anomaly (reference : 1971-2000 of 20C3M experiment) for HadCRU2 observations, 20C3M, SRES-B1, A1B and A2 simulations, respectively in black, green, orange, red and purple solid lines (11-yr running mean). Green and black dots represent yearly data respectively for the observations and 20C3M.

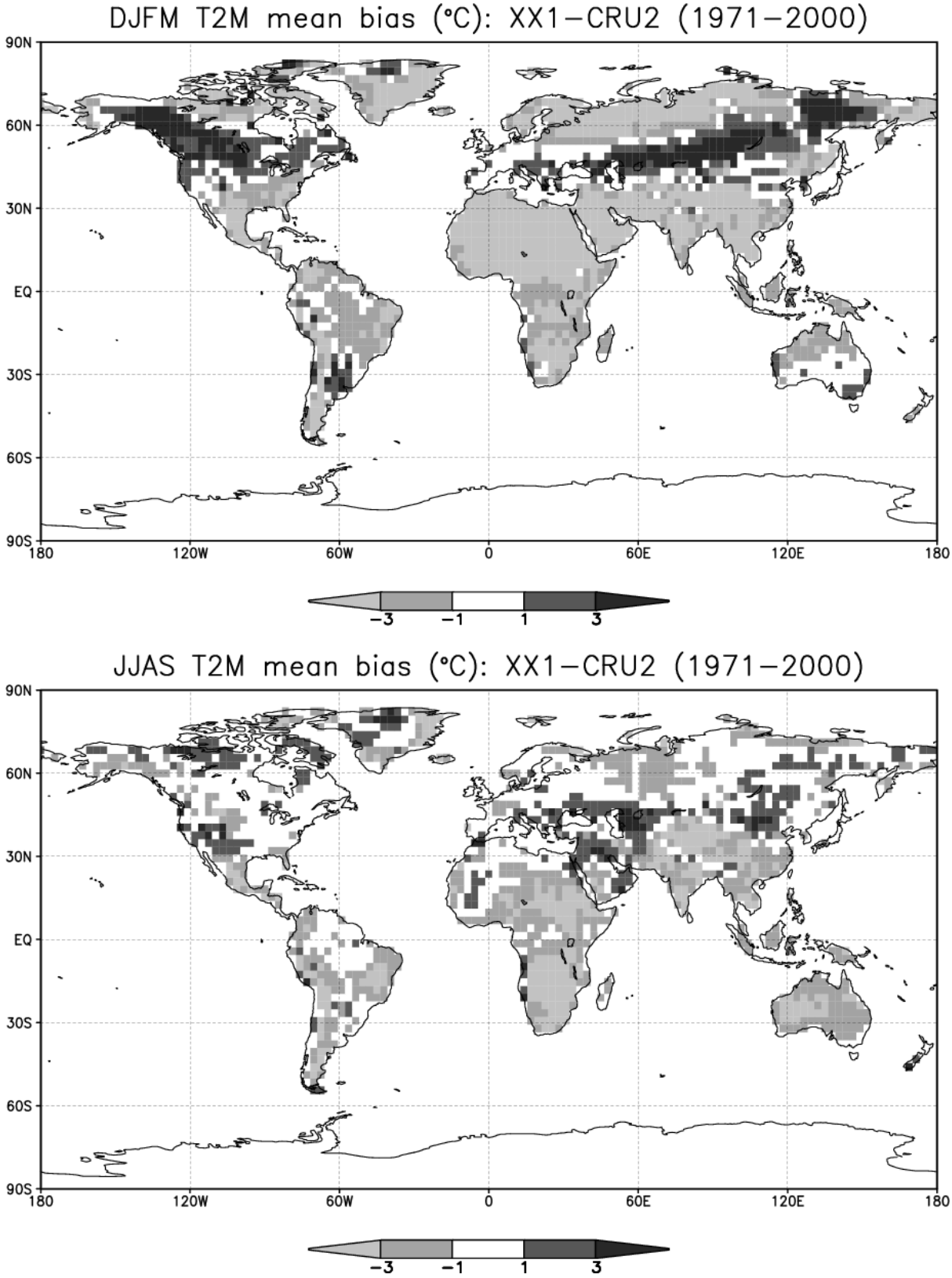

Figure 4: Modeled land T_{2m} minus CRU2 climatology (Mitchell and Jones, 2005), average on the period 1971-2000 (°C). December to March (top) and June to September (bottom).

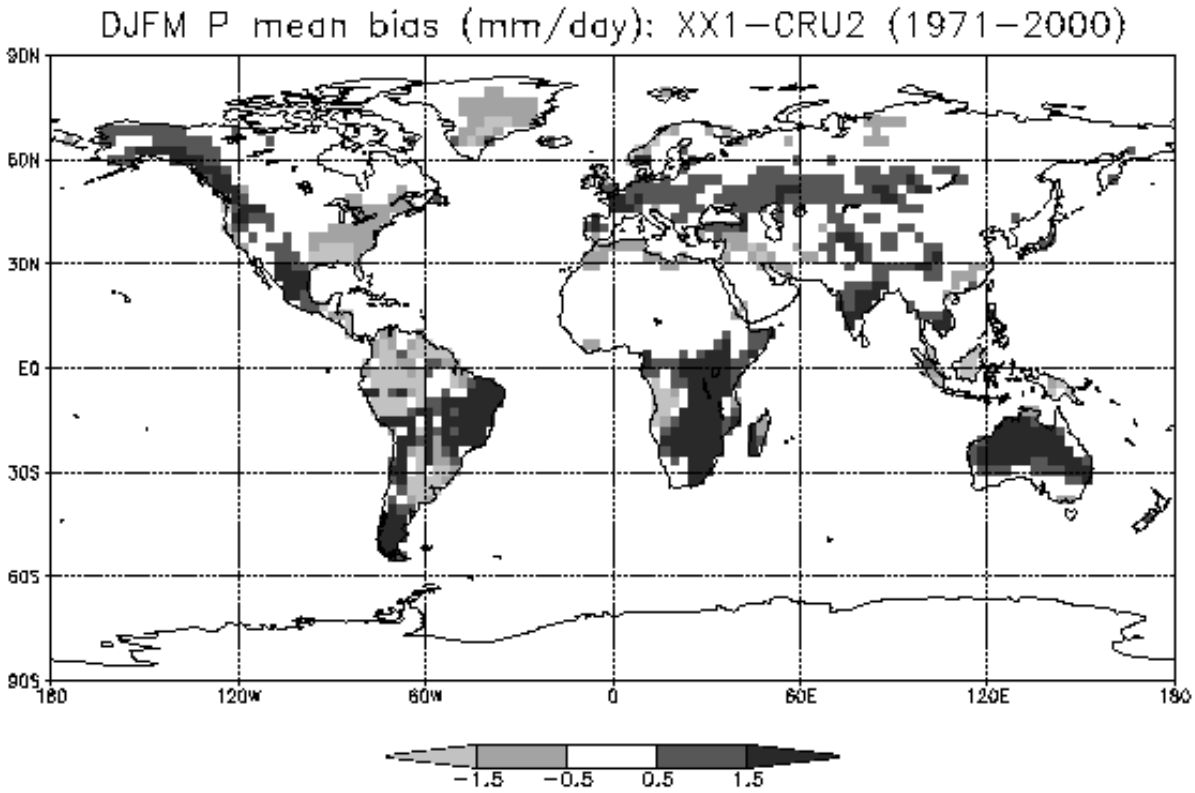

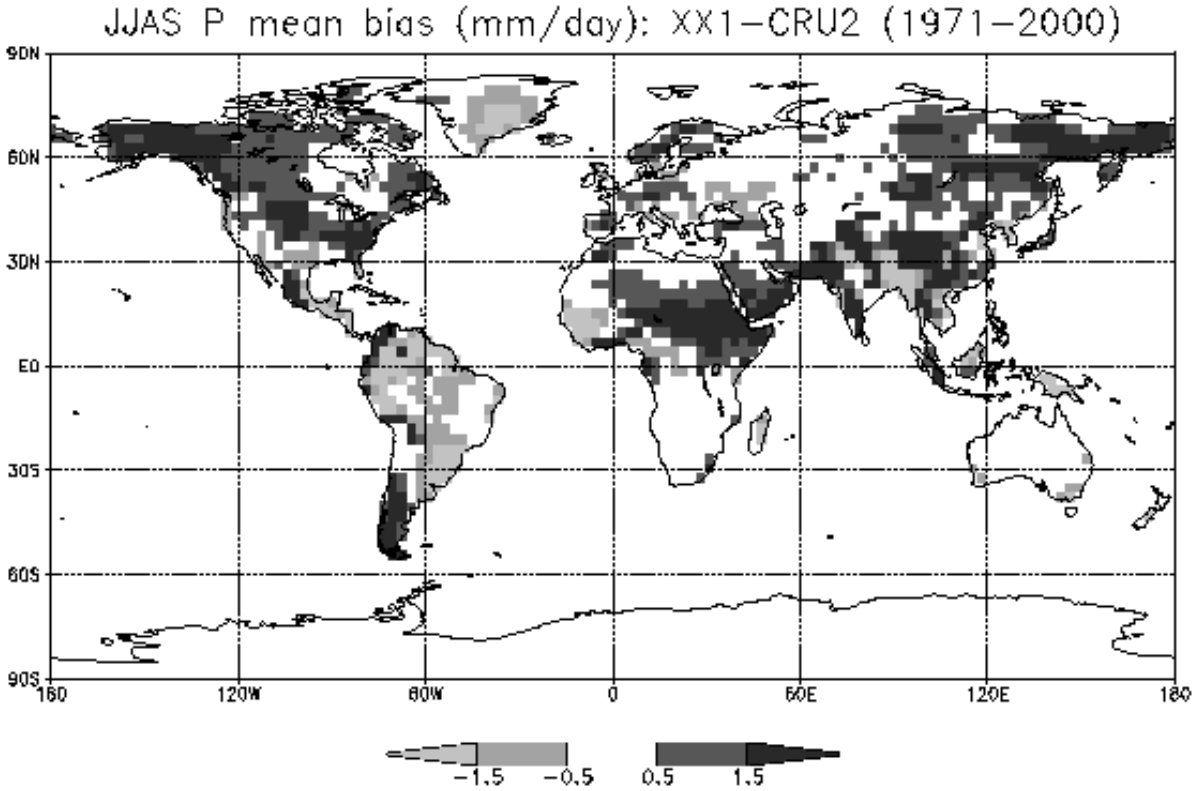

Figure 5: Same as Fig. 4, but for precipitation (mm/day).

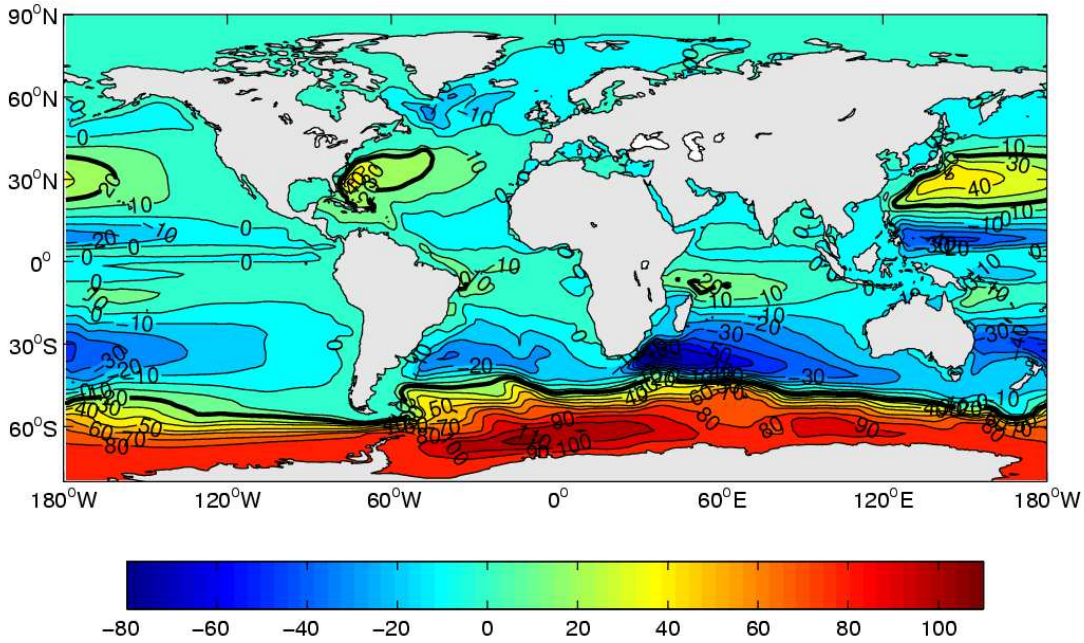

Figure 6: Barotropic stream function, average for years 1971-2000 of the 20C3M experiment.

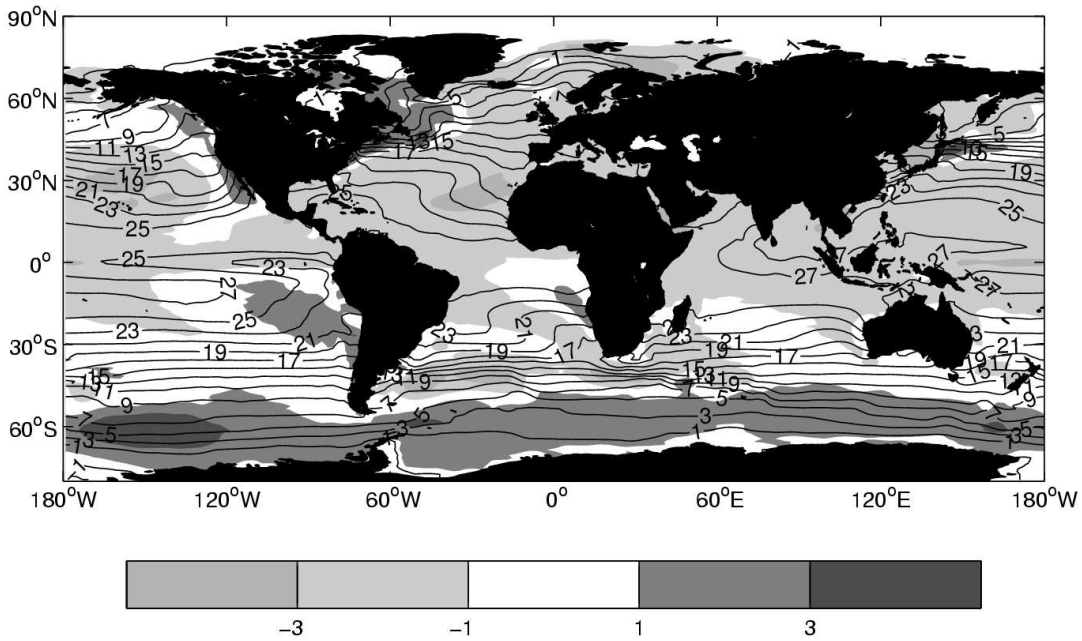

Figure 7: Contours represent modeled SST, in average for the period 1971-2000 for the 20C3M experiment. Gray-level patches represent the difference between modeled SST and HadISST.

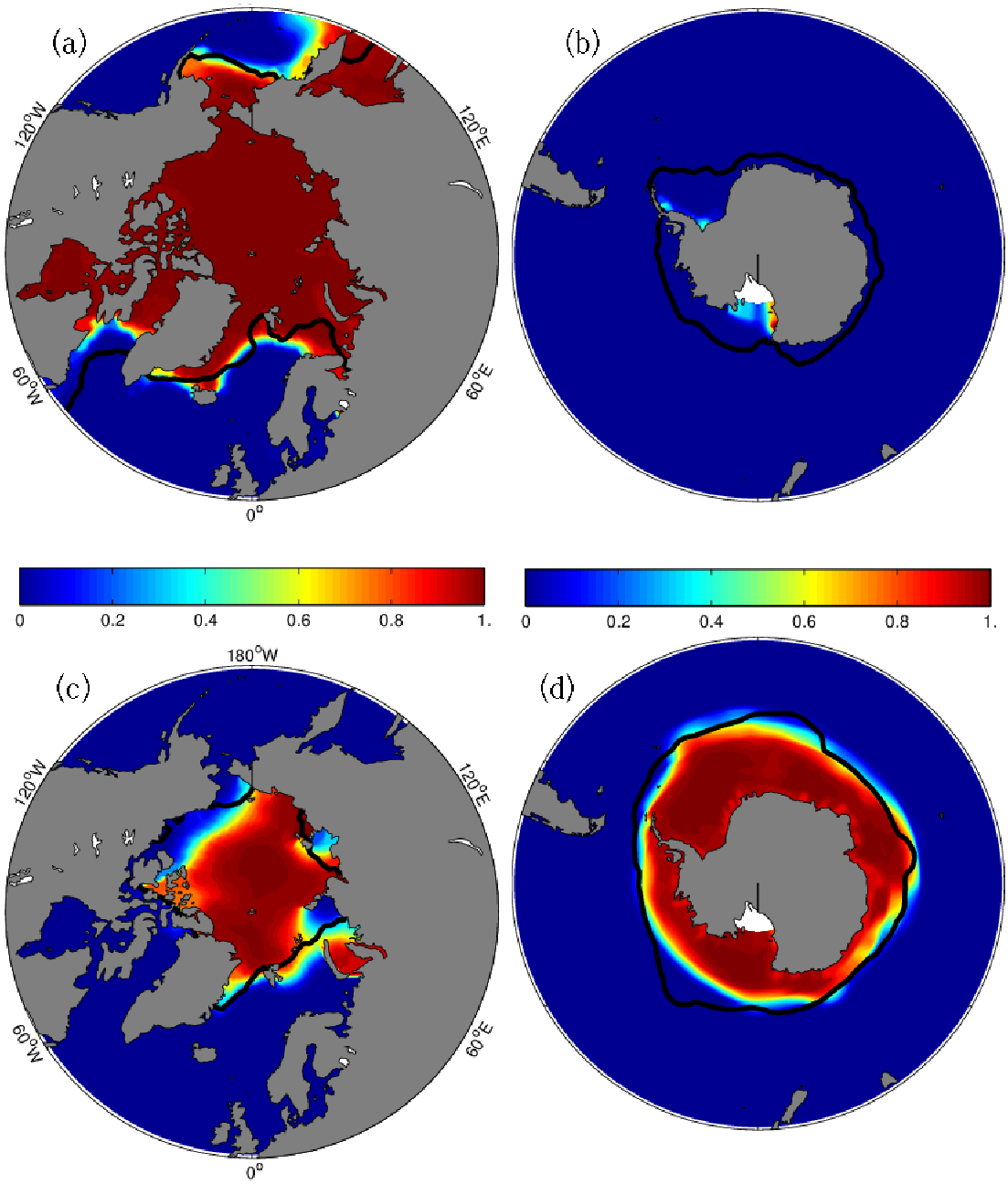

Figure 8: Average concentration of sea ice (color shaded), modelled on the period 1971-2000. (a), (b): in March, respectively for the Arctic and the Antarctic. The thick black line represents HasISST ice edge for the same period; (c) , (d): same as (a), (b), but for September.

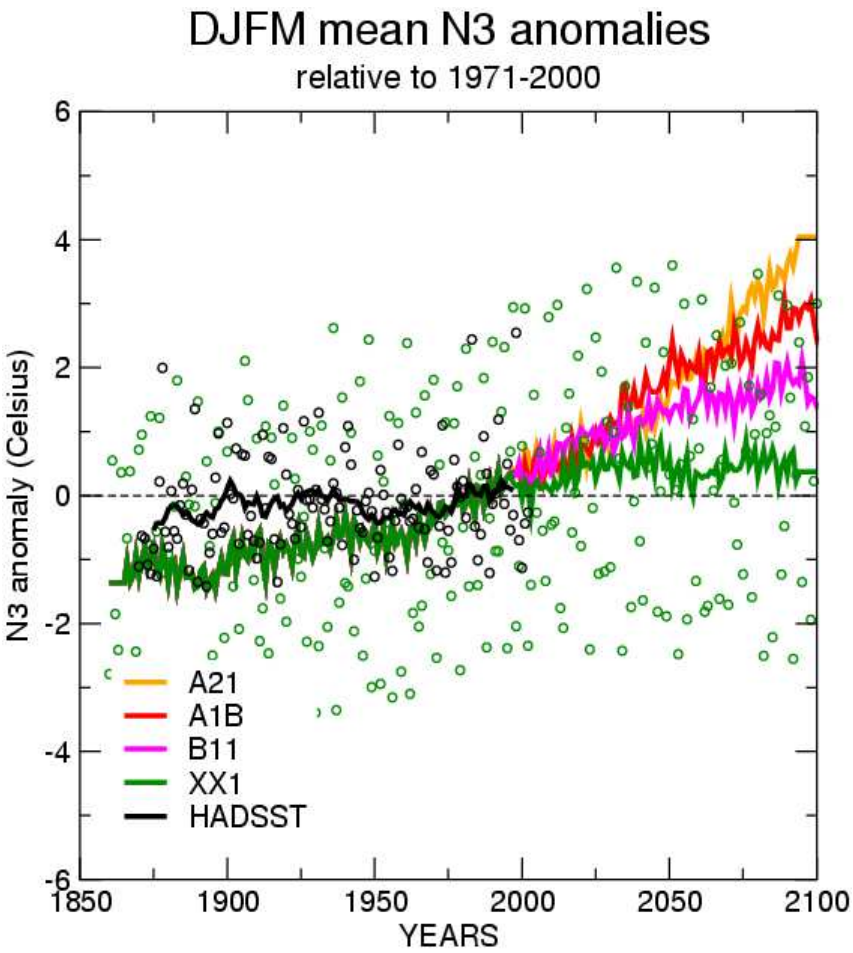

Figure 9: Nino3 box (DOMAIN) index anomaly (reference : 1971-2000 of 20C3M experiment) for HadCRU2 observations, 20C3M, SRES-B1, A1B and A2 simulations, respectively in black, green, orange, red and purple solid lines (11-yr running mean). Green and black dots represent yearly data respectively for the observations and 20C3M.

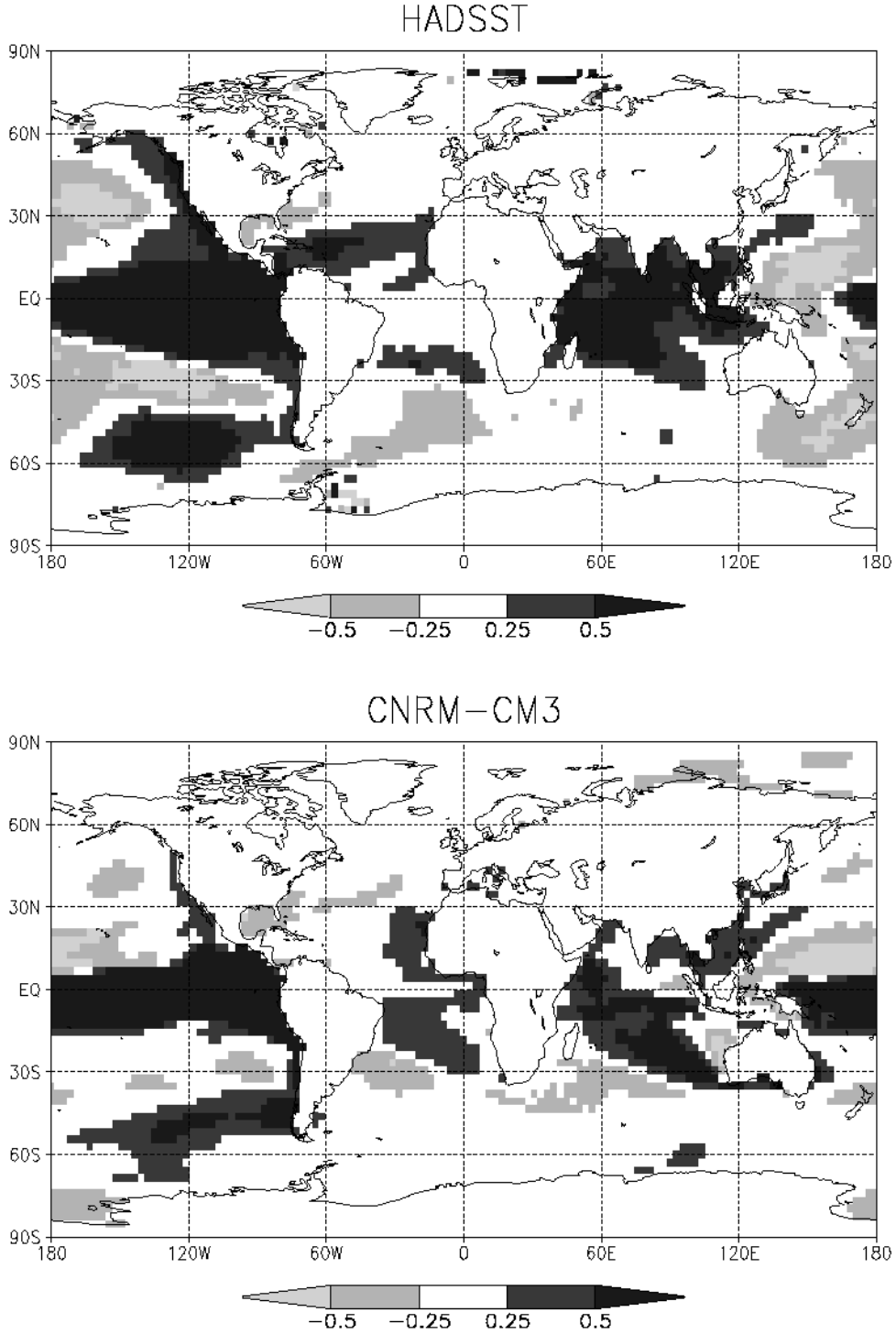

Figure 10: Correlation of ENSO3 box index with SST over the period 1951-2000, for HadISST observations (top) and the 20C3M experiment (bottom).

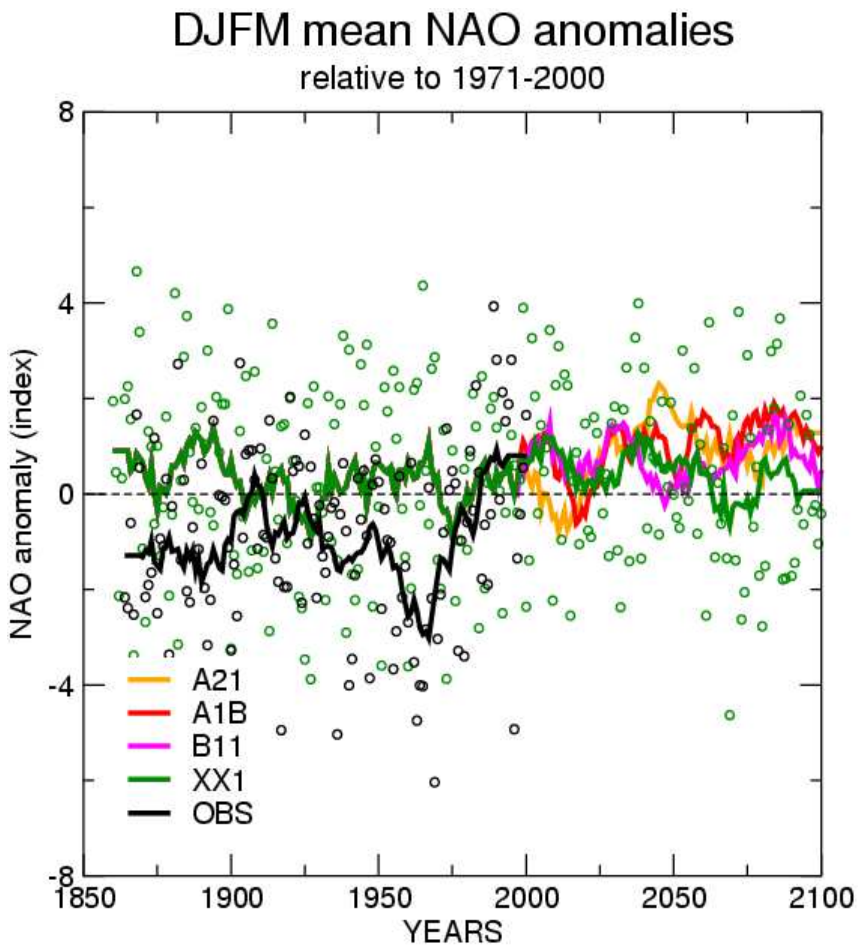

Figure 11: Same as Figure 9, but for NAO index.

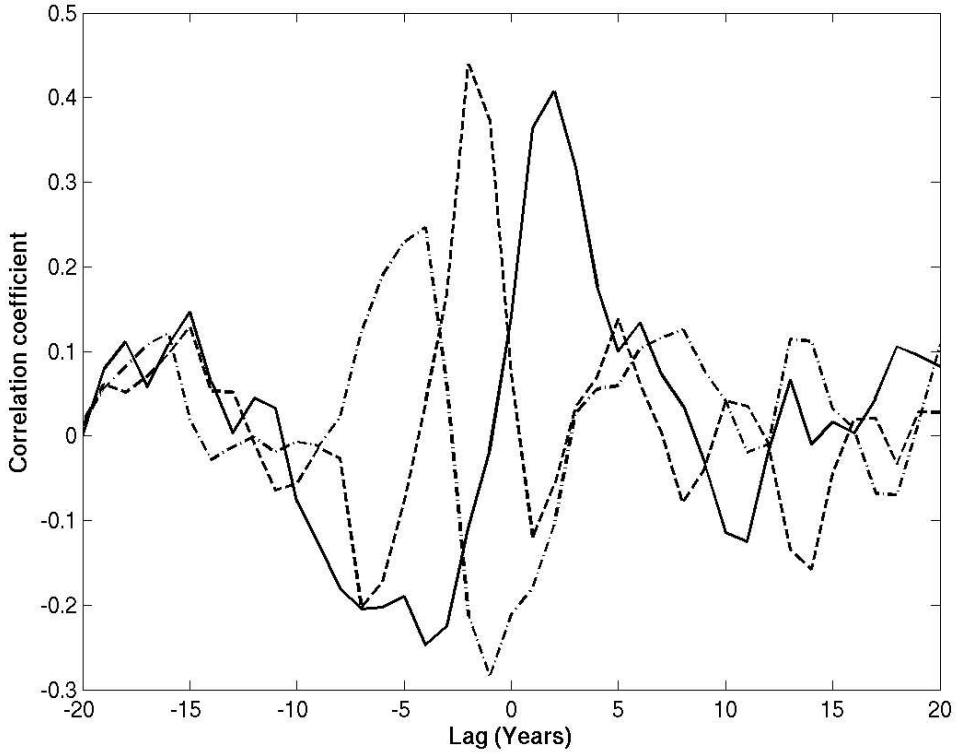

Figure 12: Lagged correlation of the THC index with ocean convection depth in Greenland-Iceland-Norwegian Seas (dash-dotted), ocean convection depth in Labrador Sea (dashed) and SST averaged on the 50°W-10°W / 40°N-60°N box. Positive lags indicate that the THC leads.

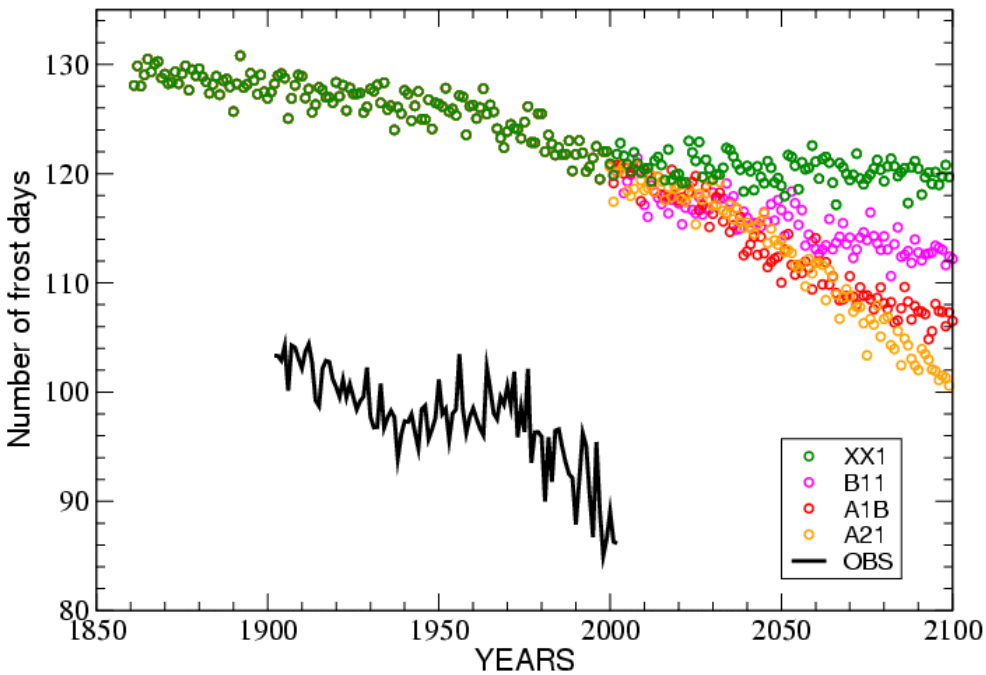

Figure 13: Global land average number of frost days. Observations, from CRU2 dataset, span the period 1902-2002 (thick line). The full, dashed, dotted and dash-dotted lines respectively represent the same quantity, but for the 20C3M experiment and its continuation ("committed", from 2001 to 2100), the SRES-B1, the SRES-A1B and the SRES-A2 scenarios.

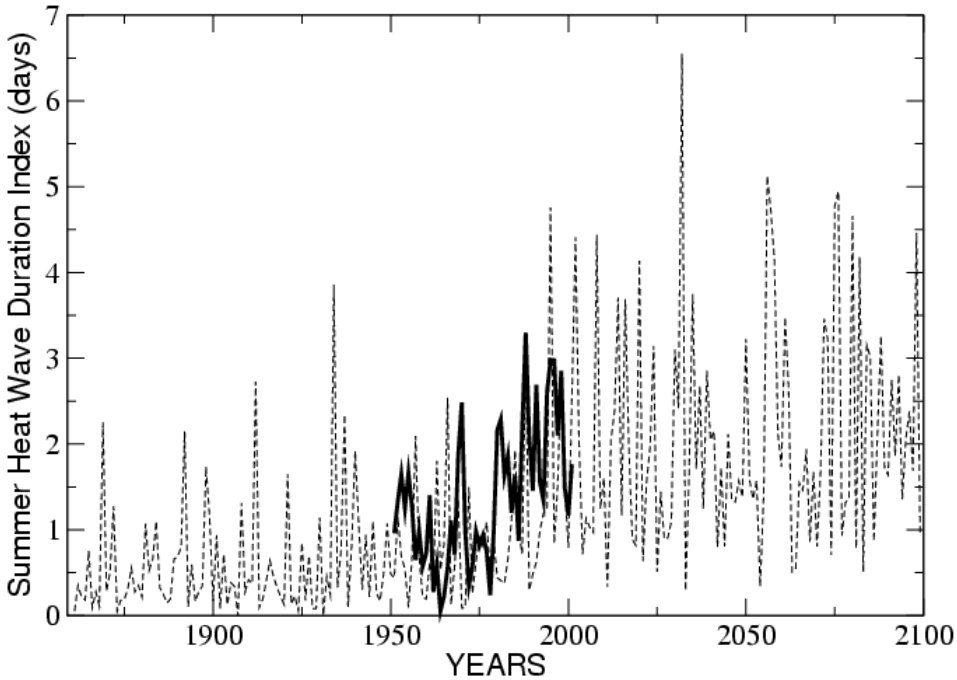

Figure 14: Spatially averaged summer heat wave index for North America. Model 20C3M+commit (dashed line) and reconstruction data by Eischeid *et al.* (2000)

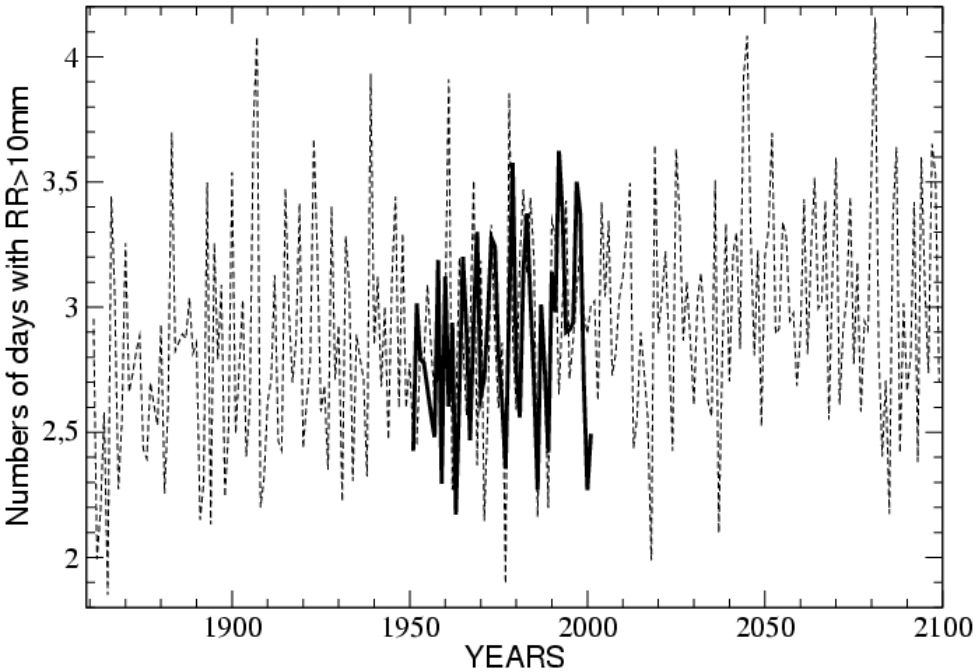

Figure 15: Number of days with daily precipitations exceeding 10mm in North America. Model 20C3M+commit (dashed line) and reconstruction data by Eischeid *et al.* (2000)

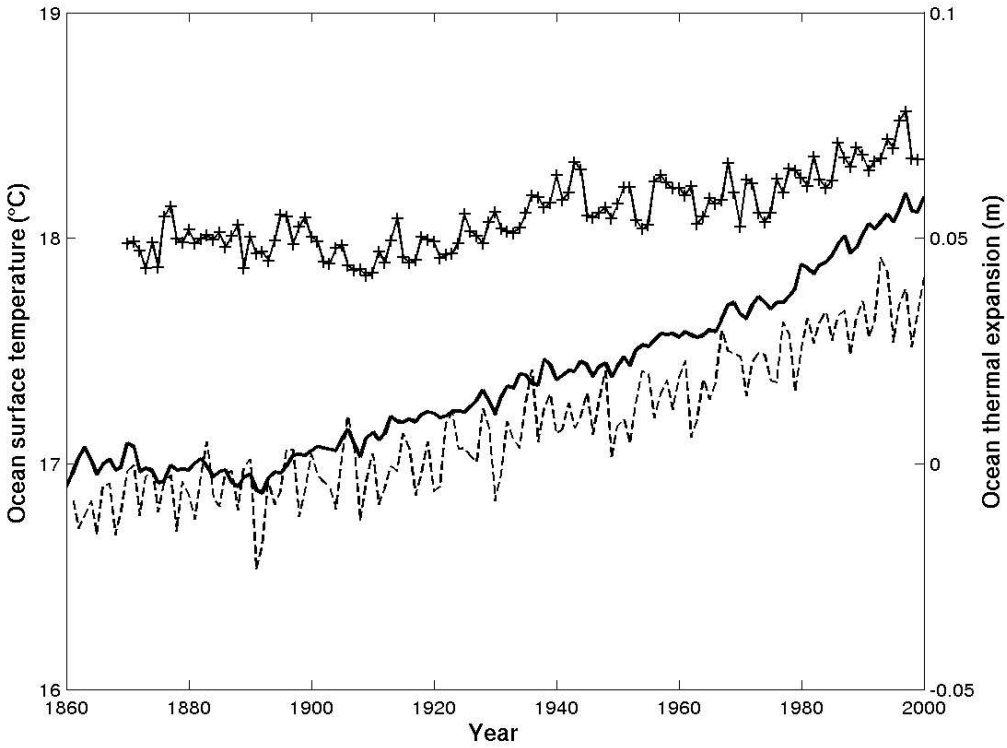

Figure 16: Modeled (20C3M experiment) and observed (HadSST) global average SST, respectively plotted as a dashed and full line (+). The global average sea level rise is represented by the bold line.